Low Temperature Physics/Fizika Nizkikh Temperatur, 2020, v. 46, No. 1, pp. 3–32

Low-temperature MnBi alloys: electronic and magnetic properties, constitution, morphology and fabrication

(Review Article)

V.N. Antonov[1,2] and V.P. Antropov[2]

[1]*G.V. Kurdyumov Institute for Metal Physics of the NAS of Ukraine, 36 Vernadsky Str., Kiev 03143, Ukraine*
E-mail: antonov@imp.kiev.ua

[2]*Ames Laboratory USDOE, Ames, IA 50011, USA*

Received May 13, 2019, published online November 25, 2019

The article reviews the rich phenomena of physical properties of MnBi. The diverse phenomena include strong spin-orbit interaction, anomalous temperature dependence of the coercivity and the magneto-crystalline anisotropy field, unique magneto-optical properties. Issues addressed include the nature of the electronic ground states of MnBi, the electronic and magnetic structures, Fermi surface, magneto-crystalline anisotropy, x-ray magnetic dichroism. The discussion includes key experiments, such as optical and magneto-optical spectroscopic measurements, de Haas–van Alphen (dHvA) measurements, x-ray photoemission and x-ray absorption spectroscopy measurements as well as x-ray magnetic circular dichroism. The effect of the spin-orbit (SO) interaction and Coulomb repulsion U were found to be crucial for the Fermi surface, cyclotron masses, magneto-optical properties, and x-ray magnetic circular dichroism. The microscopic origin of unique magneto-crystalline anisotropy and giant Kerr effect in MnBi is analyzed in detail. The huge Kerr effect in MnBi is caused by the combination of a sizable magnetic moment on manganese, the large spin-orbit coupling of bismuth, and a strong hybridization between the manganese 3d and the bismuth 6p states. The magneto-optically active states are mainly the 6p states of Bi. We show that the observed temperature dependence of the magneto-crystalline anisotropy can be explained taking into account the spin-orbit interaction together with strong Coulomb electron-electron interaction. The SO coupling of Bi is equally responsible for the large magneto-crystalline anisotropy energy as is the exchange splitting of Mn. The fabrication, morphology, and constitution of low-temperature MnBi alloys in bulk, thin films, and nanoparticles are discussed. The nanocomposite permanent magnetic materials based on MnBi, (Co, Fe) and $Nd_2Fe_{14}B$ are also discussed.

Keywords: crystal structure, magnetocrystalline anisotropy, magneto-optical properties, x-ray magnetic circular dichroism.

Contents

1. Introduction

Nowadays hard magnetic materials are used in numerous domestic and professional appliances such as consumer electronics, computer peripherals, and telecommunications. The growing demand for miniaturization in modern technology requires the further development of hard magnetic materials. Hard magnetic materials are characterized by high coercivity, high remanence, and a high energy product. Magnetic anisotropy is essential to the realization of high coercivity, high remanence, and a high energy product.

MnBi is an intriguing ferromagnetic material, both magnetically and structurally. Manganese alloys usually tend to exhibit antiferromagnetic order, because they have nearly half-filled 3*d* bands, but MnBi is one of the few known ferromagnetic manganese compounds which can be used as a permanent magnet [1]. The other interesting magnetic properties include an extraordinarily large Kerr rotation [2], with a Curie temperature above room temperature (RT) [3], a large perpendicular anisotropy in thin films at RT [4], and a high coercivity that increases with temperature [5]. The low-temperature phase (LTP) of MnBi is ferromagnetic and has the hexagonal NiAs structure. With increasing temperature, the material remains ferromagnetic up to 628 K and then undergoes a coupled structural and magnetic phase transition to a paramagnetic high-temperature phase (HTP). The HTP is a disordered NiAs phase where 10–15% of the large bipyramidal interstitial sites are occupied by Mn atoms [6]. Rapid cooling of HTP MnBi yields a quenched high-temperature phase, which is also ferromagnetic with even larger uniaxial magneto-crystalline anisotropy energy (MAE), but smaller magnetization and Curie temperature. At RT MnBi is known to have an extremely high MAE ($K \sim 10^7$ erg/cm^3). This decreases rapidly with decreasing temperature and vanishes at 90 K (T_{SR}) [7]. The experiments indicated the presence of a spin-reorientation (SR) transition during this temperature decrease [5]. Among known hard magnetic materials, MnBi is one of few alloys where the coercive field increases with increasing temperature, reflecting the magnetic anisotropy trend.

Historically, the ferromagnetic nature of manganese-bismuth alloys was first reported by Heusler around 1904 [8]. In 1914 Bekier considered the formation of a phase MnBi as probable; the phase results from a peritectic reaction at 450 °C between pure manganese and the melted alloy containing 9% of manganese [9]. Parravano and Perretl [10] established the phase diagram for this system and isolated crystals containing 19.9% manganese, which they considered to be the MnBi phase. Hilpert and Dieckmann [11] noted the strong ferromagnetism of these alloys and placed the Curie temperature at around 360–380 °C. Furst and Halla later concluded from x-ray studies that a single compound was present with the structure Mn_2Bi [12]. Montignie, however, showed that MnBi represented the only stable compound [13]. In further studies by Halla and Montignie, the same results were obtained [14].

The most comprehensive studies of this material were performed by Guillaud in 1943 in Paris. As a part of his PhD thesis, he was the first to prepare the hexagonal MnBi compound and study its numerous magnetic properties [15]. In addition to measuring the saturation moment, MAE, and Curie temperature, he established the dependence of the high coercive force of MnBi on its magnetic anisotropy and reduced particle size. He also was first to observe the spin reorientation and a corresponding increase of magnetic anisotropy with temperature. Because of these considerations, around 60 years ago, MnBi was chosen for the investigation by the US Naval Ordnance Laboratory. As a result, a new permanent magnetic alloy “Bismanol” was developed [16]. Bismanol has very high coercive force and moderate energy density, making it a good choice for small electric motors. However, due to oxidation and corrosion problems, Bismanol has not been used much as a practical magnet.

Nevertheless, studies of both fundamental and applied properties relevant for permanent magnetism have never been abandoned and this material attracted the attention of the new generation of researchers. T. Hihara and Y. Köi [17] studied the temperature dependence of the easy axis of the magnetization in MnBi using the nuclear magnetic resonance method. They found that for high temperatures above 143 K, the easy axis of magnetization is along the c direction. As the temperature is decreased between the T_{SR1} = 143 K and T_{SR} = 90 K (spin canting interval), the polar angle θ is gradually deviates from the c axis to $\theta_{exp} \sim 37°$. The magnetization flops into the ab basal plane at 90 K. This spin reorientation was also observed by neutron diffraction [5,7] and magnetization measurements on MnBi single crystals [18].

Nearly simultaneously with Bismanol’s development, MnBi became the subject of another research activity after being recognized that, in the form of thin films, it had quite favorable properties with regard to potential applications for magneto-optical (MO) recording [19–22] (see references prior 1988 and discussion in Ref. 23). The MO properties of MnBi were measured by several authors [2,24–26]. The most extensive study was carried out by Di *et al.* [2,25]. Their measured Kerr angle spectrum for MnBi has peaks at 1.84 eV and 3.35 eV. The former has a relatively large magnitude of 2.31° at 85 K.

The electronic band structure of MnBi has been calculated by several authors [5,27–45]. The optical and MO spectra of MnBi have been calculated in Refs. 29, 30, 32, 33, 35, 45. However, there are still disagreements about the interpretation of the MO spectra. The major disagreement concerns the theoretical description of a high energy peak of the Kerr rotation observed experimentally at 3.35 eV. Köhler and Kübler [32,33] obtained only one peak at 1.8 eV. They hypothesized that the thin-film samples may

have considerable impurities from materials in contact with them. They found that oxygen, as an impurity, produced a second peak, but energies of both peaks were not in good agreement with the experiment. Ravindran *et al.* [35], on the other hand, did find a second peak in their calculated Kerr-angle spectrum for pure MnBi. Oppeneer *et al.* [30] obtained a large negative peak at 1.8 eV. This is in agreement with experiment. They then found only a shoulder around 3.4 eV. Here, the experimental data has a pronounced peak. Since the data of Di *et al.* [2,25] were taken on a sample with the composition $Mn_{1.08}Bi$, Oppeneer *et al.* [30] simulated this material and found a calculated Kerr-angle spectrum with a similar but weaker peak at 1.8 eV and a second peak at 4.3 eV. This is higher in energy than that for MnBi. The studies of MO properties of MnBi performed in the LDSA approximation provide calculations values of Mn spin magnetic moment significantly smaller in comparison with the experimental measurements.

Manganese forms a vast variety of intermetallic compounds owing to its half-filled valence shell. The unpaired electrons also make it a highly magnetically active material with an intrinsic magnetic moment. Also, Mn element is abundant in the Earth's crust and it is inexpensive to process when compared to the rare-earth (RE) elements. Among the known intermetallic compounds, Mn-based MnBi, MnAl, and MnGa, are some of the most common alloys that have been studied as potential replacements for RE magnets [46]. The LTP of MnBi alloy has shown the highest energy product (16.2 MG·Oe) among the three. For decades, much effort has been made to understand the mechanism, structures, and magnetic properties of these Mn-based magnets. However, a cohesive review has been still missing. Therefore, this review summarizes the latest advancements in Mn-based magnetic alloys across different dimensions, to intending to further push the boundary for this dynamic and critical subject. In the following, the development of MnBi alloys is discussed, containing their synthetic techniques, and structural, magnetic, and electronic properties.

The review is divided into two parts. The first part (Secs. 3–5) devoted to the theoretical investigation of the electronic and magnetic structures as well as various physical properties of MnBi. The electronic and magnetic structures, Fermi surface (FS), orbital dependence of the cyclotron masses, and extremal cross-sections of the Fermi surface, magneto-optical Kerr spectra, x-ray magnetic circular dichroism, temperature dependence of the magnetocrystalline anisotropy of MnBi have been considered. We provide a theoretical explanation for the long-standing experimental puzzles in the measured MO properties, coercivity, and spin orientation. We show that all the physical properties under consideration can be properly described only taking into account SO interaction and Coulomb electron-electron correlations. The second part (Sec. 4) presents the current status, challenges, potentials as well as the future directions for MnBi as a candidate of rare-earth free permanent magnets. We also present the information on the morphology and fabrication of MnBi in the bulk and films, the influence of the substitution by different atoms on the Mn and Bi sites. Finally, the results are summarized in Sec. 7.

2. Crystal structure and calculation details

2.1. Crystal structure

MnBi exhibits a first-order structural transition between temperatures of 613 K and 628 K [91]. The LTP possesses the desired magnetic properties. Researchers also refer to this phase as α-MnBi. The Mn–Bi phase diagram is shown in Fig. 1 [6]. Key phase transformations are:

1) at 628 K upon heating, α-MnBi → $Mn_{1.08}Bi$ + Bi-rich liquid;

2) at 719 K upon heating $Mn_{1.08}Bi$ → Mn + Bi-rich liquid;

3) at 613 K during cooling $Mn_{1.08}Bi$ → α-MnBi + Mn;

4) at 535 K during cooling, MnBi + Bi → Bi-rich liquid.

Currently the generally accepted composition, lattice structure and parameters for the high temperature phase (β-MnBi) at 630 K are $Mn_{2.23}Bi_{1.88}$, *Pmma* symmetry, and $a = 5.959$ Å, $b = 4.334$ Å, $c = 7.505$ Å, $\alpha = \beta = \gamma = 90°$ [47]. For the LTP phase (α-MnBi) at 300 K, they are $Mn_{50}Bi_{50}$, $P6\bar{3}/mmc$ symmetry, (group number 194), and $a = b = 4.290$ Å, $c = 6.126$ Å, $\alpha = \beta = 90°$, $\gamma = 120°$. For the α-MnBi at 20 K, they are $Mn_{50}Bi_{50}$, *Cmcm* symmetry, and $a = 4.269$ Å, $b = 7.404$ Å, and $c = 6.062$ Å, $\alpha = \beta = \gamma = 90°$.

The magnetic structure of MnBi goes through a spin-reorientation process with temperature increasing from 0 K. Neutron and x-ray diffraction measurements [48,49] showed that the magnetic easy axis of MnBi is in-plane at lower temperature and starts to reorient out-of-plane to *c*-axis at about 90 K, and completely aligned with *c*-axis when temperature is above 150 K (see Fig. 2). Zarkevich *et al.* estimated the magnetic moment at 0 K as $3.96\mu_B$ with site-projected moments of 4.231 and $-0.273\mu_B$ on Mn and Bi,

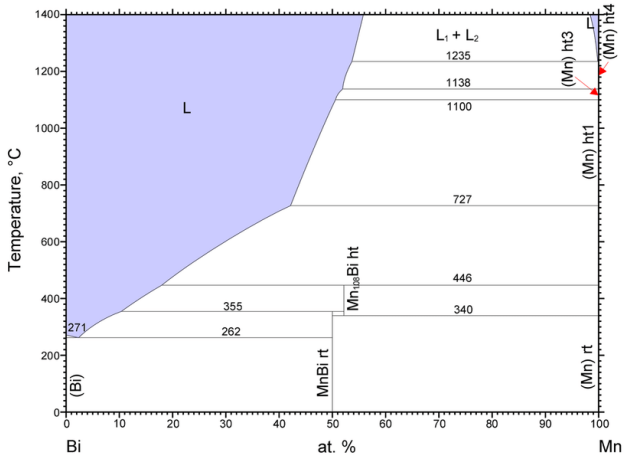

Fig. 1. Mn–Bi phase diagram [6] (www.asminternational.org).

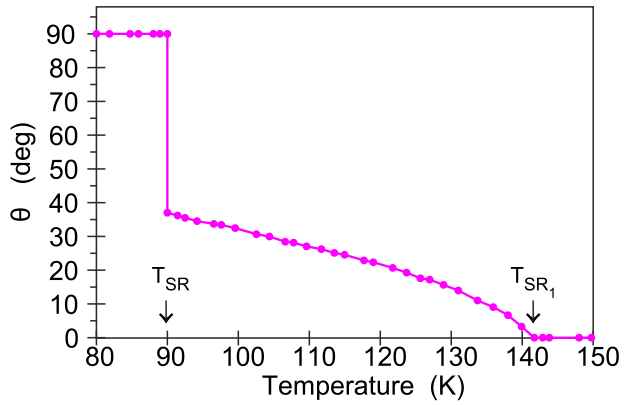

Fig. 2. (Color online) Temperature variation of the polar angle θ between the easy axis of the magnetization and the *c*-axis in MnBi [17].

respectively [50]. Andresen *et al.* [7] also showed that above the transition between 613 and 633 K, 15% of the Mn atoms have left their regular lattice sites and occupied the large trigonal bipyramidal holes of the NiAs structure. This also explains the observed contraction of the *c*-axis.

Figure 3 depicts the crystal and magnetic structure of LT α-MnBi. It exhibits large trigonal-bipyramidal interstitial sites, which may be occupied by dopant or Mn atoms. It is speculated that octahedral Mn atoms are ferromagnetically coupled with the spin parallel to the *c*-axis, and the bipyramidal Mn atoms are antiferromagnetically coupled to the octahedral Mn atoms and result in reduced net magnetization [7,51].

2.2. Magneto-crystalline anisotropy

The internal energy of ferromagnetic materials depends on the direction of spontaneous magnetization. Here we consider one part of this energy, the MAE, which possesses the crystal symmetry of the material. For the material exhibiting uniaxial anisotropy, such as a hexagonal crystal, the MAE can be expressed as [52]

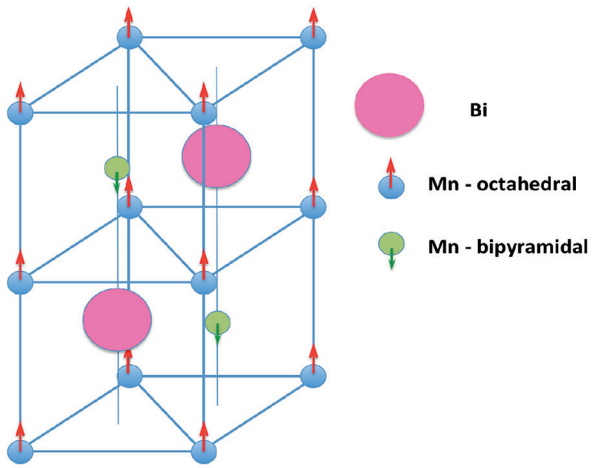

Fig. 3. (Color online) Crystal lattice of MnBi LTP phase.

$$K = K_1 \sin^2\theta + K_2 \sin^4\theta + K_3' \sin^6\theta + \\ + K_3 \sin^2\theta \cos[6(\phi+\psi)] + ..., \quad (1)$$

where K_i is the anisotropy constant of the ith order, θ and ϕ are the polar angles of the Cartesian coordinate system where the c axis coincides with the z axis (the Cartesian coordinate system was chosen such that the x axis is rotated through 90° from the a hexagonal axis) and ψ is the phase angle.

Here, we consider MAE caused only by the SO interaction and define it as the difference between two self-consistently calculated relativistic total energies for two different magnetic field directions, $K = E(\theta) - E(\langle 0001 \rangle)$.

2.3. Magneto-optical properties and x-ray magnetic circular dichroism

For the polar Kerr magnetization geometry and a crystal of tetragonal symmetry, where both the fourfold axis and the magnetization **M** are perpendicular to the sample surface and the z-axis is chosen to be parallel to them, the dielectric tensor is composed of the diagonal ε_{xx} and ε_{zz}, and the off-diagonal ε_{xy} components in the form

$$\varepsilon = \begin{pmatrix} \varepsilon_{xx} & \varepsilon_{xy} & 0 \\ -\varepsilon_{xy} & \varepsilon_{xx} & 0 \\ 0 & 0 & \varepsilon_{zz} \end{pmatrix}. \quad (2)$$

The various elements $\hat{\varepsilon}_{\alpha\beta}$ are composed of real and imaginary parts as follows: $\hat{\varepsilon}_{\alpha\beta} = \varepsilon^{(1)}_{\alpha\beta} + i\varepsilon^{(2)}_{\alpha\beta}$, where $\alpha, \beta \equiv x, y, z$, $\varepsilon_{xx} = (n+ik)^2$, n and k are refractive index and extinction coefficient, respectively. The optical conductivity tensor $\hat{\sigma}_{\alpha\beta} = \sigma^{(1)}_{\alpha\beta} + i\sigma^{(2)}_{\alpha\beta}$ is related to the dielectric tensor $\varepsilon_{\alpha\beta}$ through the equation

$$\hat{\varepsilon}_{\alpha\beta}(\omega) = \delta_{\alpha\beta} + \frac{4\pi i}{\omega}\hat{\sigma}_{\alpha\beta}(\omega). \quad (3)$$

The Kerr rotation θ and ellipticity η are expressed as follow [53]:

$$\theta + i\eta \approx \frac{-\varepsilon_{xy}}{(\varepsilon_{xx}-1)\sqrt{\varepsilon_{xx}}}. \quad (4)$$

The optical conductivity of MnBi has been computed from the energy band structure using the Kubo–Greenwood [54] linear-response expression [55]:

$$\sigma_{\alpha\beta}(\omega) = \frac{-ie^2}{m^2\hbar V_{uc}} \times \\ \times \sum_{\mathbf{k}} \sum_{nn'} \frac{f(\varepsilon_{n\mathbf{k}}) - f(\varepsilon_{n'\mathbf{k}})}{\omega_{nn'}(\mathbf{k})} \frac{\Pi^{\alpha}_{n'n}(\mathbf{k})\Pi^{\beta}_{nn'}(\mathbf{k})}{\omega - \omega_{nn'}(\mathbf{k}) + i\gamma}, \quad (5)$$

where $f(\varepsilon_{n\mathbf{k}})$ is the Fermi function, $\hbar\omega_{nn'}(\mathbf{k}) \equiv \varepsilon_{n\mathbf{k}} - \varepsilon_{n'\mathbf{k}}$ is the energy difference of the Kohn–Sham energies, $\varepsilon_{n\mathbf{k}}$,

and γ is the lifetime parameter, it is included to describe the finite lifetime of the excited Bloch electron states. The $\Pi_{nn'}^{\alpha}$ are the dipole optical transition matrix elements. In a fully relativistic description, these are given by

$$\Pi_{nn'}(\mathbf{k}) = \langle \psi_{n\mathbf{k}} \mid c\alpha \mid \psi_{n'\mathbf{k}} \rangle \qquad (6)$$

with the four-component Bloch electron wave function $\psi_{n\mathbf{k}}$, velocity of light c, and Dirac operator α. The combined correction terms were also taken into account in the optical matrix element calculations. A detailed description of the optical matrix elements in the Dirac representation is given in Refs. 56, 57.

Within the one-particle approximation, the absorption coefficient $\mu_j^{\lambda}(\omega)$ for incident x-ray of polarization λ and photon energy $\hbar\omega$ can be determined as the probability of electronic transitions from initial core states with the total angular momentum j to final unoccupied Bloch states

$$\mu_{\lambda}^{j}(\omega) = \sum_{m_j}\sum_{n\mathbf{k}} |\langle \Psi_{n\mathbf{k}} \mid \Pi_{\lambda} \mid \Psi_{jm_j} \rangle|^2 \, \delta(E_{n\mathbf{k}} - E_{jm_j} - \hbar\omega) \times$$
$$\times \theta\,(E_{n\mathbf{k}} - E_F), \qquad (7)$$

where Ψ_{jm_j} and E_{jm_j} are the wave function and the energy of a core state with the projection of the total angular momentum m_j; $\Psi_{n\mathbf{k}}$ and $E_{n\mathbf{k}}$ are the wave function and the energy of a valence state in the nth band with the wave vector $\mathbf{k}$; E_F is the Fermi energy. $\Pi_{\lambda} = -e\boldsymbol{\alpha}\mathbf{a}_{\lambda}$ is the electron–photon interaction operator in the dipole approximation (6), $\mathbf{a}_{\lambda}$ is the λ polarization unit vector of the photon vector potential, with $a_{\pm} = 1/\sqrt{2}(1, \pm i, 0)$, $a_{\parallel} = (0,0,1)$. Here, "+" and "–" denotes, respectively, left and right circular photon polarizations concerning the magnetization direction in the solid. X-ray magnetic circular and linear dichroisms are given then by $(\mu_+ - \mu_-)$ and $(\mu_{\parallel} - (\mu_+ + \mu_-)/2)$, respectively.

Usually, the exchange splitting of a core-shell is small compared to the bandwidth of final valence states and can be neglected. However, the exchange splitting of the $2p_{1/2,3/2}$ states of 3*d* transition metals may be as large as 0.4 eV. Then, transitions from core states with different m_j in Eq. (7) occur at different photon frequencies. This may lead to the appearance of giant x-ray magnetic linear dichroism (XMLD) in cubic 3*d* metals and it's strong dependence on the magnetization direction [58].

At the core level, x-ray magnetic circular dichroism (XMCD) is not only element-specific but also orbital specific. For 3*d* transition metals, the electronic states can be probed by the K, $L_{2,3}$ and $M_{2,3}$ x-ray absorption and emission spectra. In Bi, one can use the K, $L_{2,3}$, $M_{2,3}$, $M_{4,5}$, $N_{2,3}$, $N_{4,5}$, $N_{6,7}$, and $O_{2,3}$ spectra. For unpolarized absorption spectra $\mu^0(\omega)$ allows only transitions with $\Delta l = \pm 1$, $\Delta j = 0, \pm 1$ (dipole selection rules). Therefore only electronic states with an appropriate symmetry contribute to the absorption and emission spectra under consideration.

2.4. Treatment of the Coulomb correlations

It is well known that the local spin-density approximation (LSDA) fails to describe the electronic structure and properties of the systems in which the interaction among the electrons is strong. In recent years, more advanced methods of electronic structure determination such as LSDA plus self-interaction corrections [59], the LSDA+U [60] method, GW approximation [61], and dynamical mean-field theory [62–64] have sought to remedy this problem and have shown considerable success. Among them, the LSDA+U method is the simplest and most frequently used. We used the "relativistic" generalization of the rotationally invariant version of LSDA+U method [65], which takes into account SO coupling so that the occupation matrix of localized electrons becomes non-diagonal in spin indexes.

The screened Coulomb U and exchange J integrals enter the LSDA+U energy functional as external parameters and have to be determined independently. The value of U can be estimated from the photoemission spectroscopy and x-ray Bremsstrahlung isochromatic spectroscopy experiments. Because of difficulties with unambiguous determination of U it can be considered as a parameter of the model. Its value can, therefore, be adjusted to achieve the best agreement of the results of LSDA+U calculations with photoemission or optical spectra [66]. While the use of an adjustable parameter is generally considered an anathema among first principles practitioners, the LSDA+U approach does offer a plausible and practical method to approximately treat strongly correlated orbitals in solids. The Hubbard U and exchange parameter J can be determined from supercell LSDA calculations using Slater's transition state technique [67,68] or from constrained LSDA calculations (cLSDA) [68–70]. Recent extensions of the cLSDA method may be found in Refs. 71, 72. The cLSDA method, however, is known from early on to yield values of U that are too large in some cases [73]. For example, Anisimov and Gunnarsson [67] computed the effective on-site Coulomb interaction in metallic Fe and Ce. For Ce, the calculated Coulomb interaction was found to be about 6 eV in good agreement with empirical and experimental estimates ranging from 5 to 7 eV. The result for Fe (also about 6 eV) was surprisingly high since U was expected to be in the range of 2–3 eV for elemental transition metals, except for Ni [74,75]. The cLSDA method applied to MnBi produces U = 4.57 eV, J = 0.97 eV [45].

Another method for determining the effective interaction is a scheme based on the random-phase approximation (RPA). Early attempts of this can be found in Refs. 76, 77. A method for calculating the Hubbard U, called the constrained RPA (cRPA) scheme was proposed by Aryasetiawan *et al.* [78]. Subsequently, a combined cLSDA and cRPA method was also proposed [79]. The main merit of the cRPA method over currently available methods is that

it allows for a precise elimination of screening channels. They are instead to be included in a more sophisticated treatment of the model Hamiltonian [80]. This method allows easy access to obtaining not only on-site matrix elements but also off-site matrix elements as well as screened-exchange matrix elements. These are usually taken to be the atomic value. Another merit is the possibility of obtaining the frequency-dependent Hubbard U, and may prove to be important. The cRPA method has now been applied to several systems with success [73,81–83].

Authors of Ref. 45 tried several approximations to obtain Hubbard U and J, they found that the values $U = 4$ eV and $J = 0.97$ eV are most appropriate to describe the electronic structure and various physical properties of MnBi.

3. Energy band structure

Figure 4 shows the spin-polarized energy band structure of MnBi calculated in the LSDA without SO interaction (two upper panels), fully relativistic Dirac approximation (LSDA+SO, third panel from the top), and a fully relativistic Dirac LSDA+SO+U approximation (lower panel) [45]. In "fat band" representation, the open red circles show the Mn 3d character of the wave function in each **k** point. Closed blue circles indicate the Bi 6p character. The larger circle corresponds to the larger contribution of the corresponding character in the wave function for a given **k** point.

The splitting of the energy bands in the H and A symmetry point in the –0.6 eV to –1 eV energy interval is enhanced more than two times after the inclusion of the Coulomb repulsion (compare third panel from the top with lower panel in Fig. 4). Due to the shift of Mn 3d states from the Fermi level in the LSDA+SO+U approach, the character of the electronic states at the Fermi level are changed towards the decreasing of an Mn 3d partial contribution at the Fermi level.

Figure 5 shows partial densities of states for MnBi calculated within LSDA+SO as well as LSDA+SO+U [45]. The Mn d-states are split by the on-site exchange interaction into nearly completely filled majority-spin and unoccupied minority-spin states. The crystal field at the Mn site (D_{3d} point symmetry) causes the splitting of d-orbitals into a singlet a_{1g} ($3z^2 - 1$) and two doublets e_g (yz and xz) and e_{g1} (xy and $x^2 - y^2$). Bi 6s states situated at the –12.2 to –10.3 eV below the Fermi level. Bi 6p states occupy the –5.2 to 7.5 eV energy range and strongly hybridize with Mn 3d states in the –4 to 3 eV energy range. The spin splitting of Bi p-states is quite small. The LSDA+U Mn 3d partial DOSs are also presented in Fig. 5. Usually, the failure of the LSDA method generally occurs toward the right end of the 3d transition-metal series. For Mn, which is in the middle of 3d series, no strong correlation would be expected. As can be seen below, however, the correlation effects are quite important in MnBi for a correct description of the MO properties as well as the MAE.

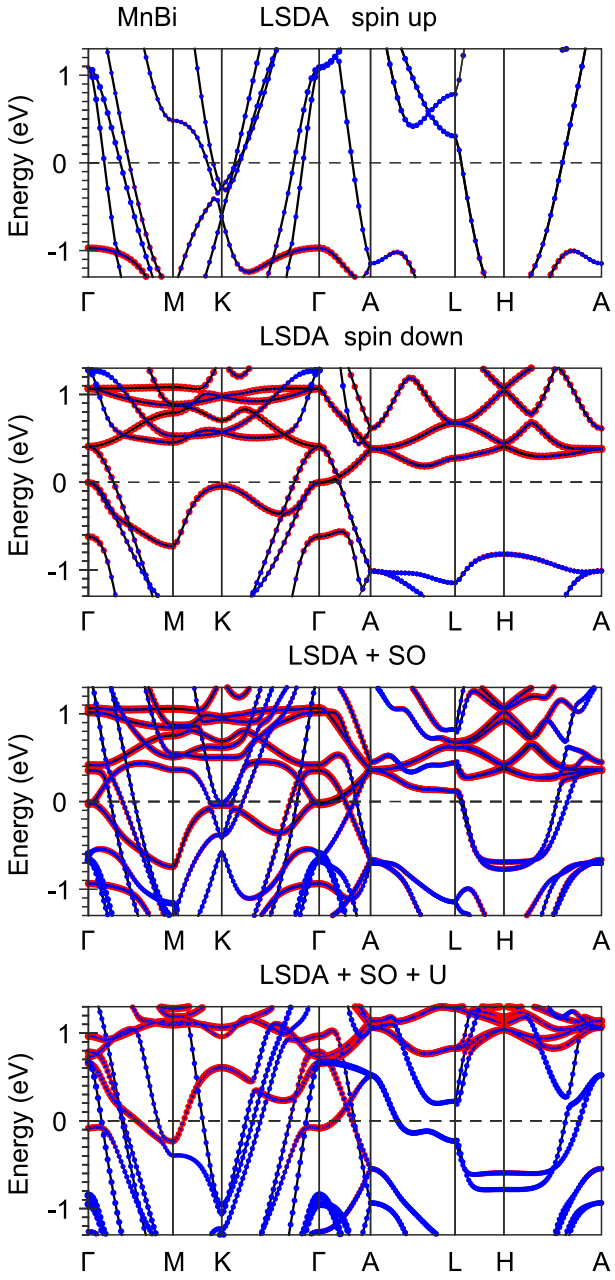

Fig. 4. (Color online) Energy band structure of MnBi in close vicinity of the Fermi level using "fat band" representation: a non-relativistic (two upper panels); fully relativistic (third panel from the top) and fully relativistic LSDA+SO+U (lower panel) energy bands [45].

Our fully relativistic LSDA band structure calculations produce M_s of $3.572\mu_B$ at the Mn site in MnBi. The M_s of $-0.114\mu_B$ induced at the Bi site is antiparallel to that of Mn. The orbital magnetic moment (M_l) at the Mn and Bi sites are equal to 0.156 μ_B and –0.028 μ_B, respectively. An additional empty sphere also carries small M_s and M_l of $-0.015\mu_B$ and 0.001 μ_B, respectively. The net magnetic moment in the fully relativistic LSDA band structure calculations is equal to $3.572\mu_B$. Experimental numbers have been obtained for different samples and samples of dif-

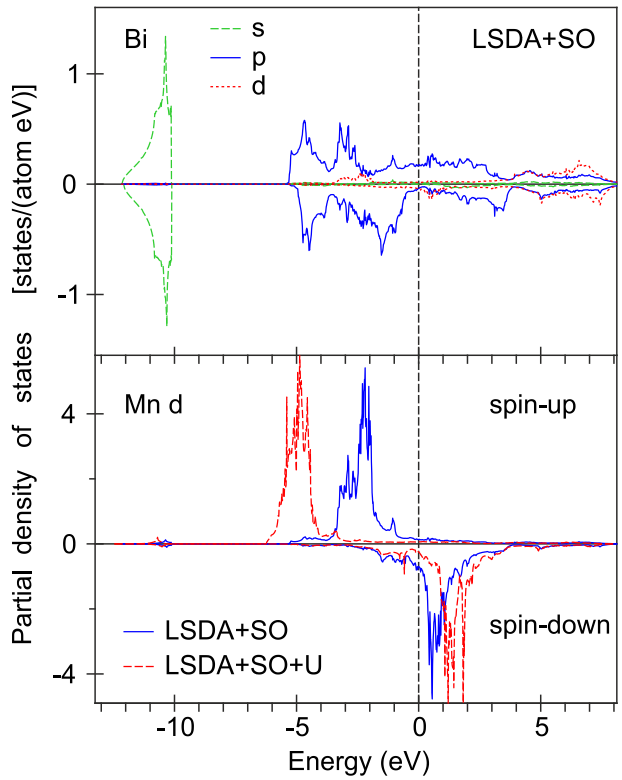

Fig. 5. (Color online) The LSDA+SO and LSDA+SO+*U* partial densities of states for MnBi [45].

ferent purity in a range from 3.82μ_B [84], to 4.25μ_B [85]. For most pure samples, the moment is close to 4.1μ_B and compares favorably with our LSDA+SO+*U* moment (4.172μ_B). The spin and orbital magnetic moments in the LSDA+SO+*U* approach at the Mn site are equal to 4.224μ_B and 0.125μ_B, respectively, and $M_s = -0.134\mu_B$ and $M_l = -0.030\mu_B$ at the Bi site [45].

The opposite sign of M_s on Mn and Bi atoms can be understood already from Fig. 4. In the LSDA, the DOS of Mn *d*-states near the Fermi level is much larger for a nearly empty spin down electronic band. The latter band just starts to populate in Mn reflecting typical more-than-half-filled *d*-band behavior. For *p*-states of Bi (upper panel of Fig. 4) the situation is opposite: the population of *p*-states and their induced magnetic moments are relatively small, with a larger DOS for *p*-states for spin up.

The presence of a large amount of Mn spin down and Bi spin up electrons at and near the Fermi level creates favorable conditions for the appearance of the large transversal $p-d$ transitions induced by SO coupling.

4. Ground state properties

4.1. Fermi surface

In this section, we present the topology of the Fermi surface of MnBi as well as the de Haas–van Alphen (dHvA) extremal cross-sections and cyclotron masses.

Figure 6 shows the calculated cross-sectional areas of MnBi FS in the plane perpendicular to the *z* direction

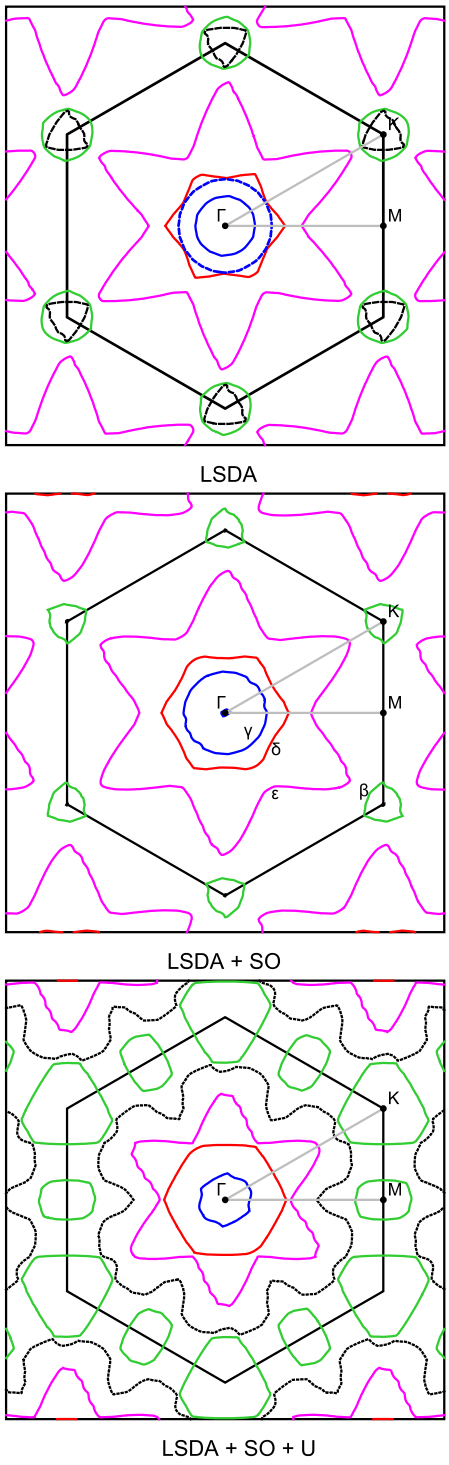

Fig. 6. (Color online) The calculated cross sections of MnBi FS in the plane perpendicular to the *z* direction $k_z = 0$ using a non-relativistic approach (upper panel), LSDA+SO (middle panel) and LSDA+SO+*U* (*U* = 4 eV) (lower panel) [45].

$k_z = 0$ crossed Γ symmetry point using a non-relativistic method (upper panel), fully relativistic LSDA+SO (middle panel) and fully relativistic LSDA+SO+*U* (lower panel) approximations [45]. Figure 7 shows the sheets of the FS in MnBi calculated with the LSDA+SO (left panels) and LSDA+SO+*U* (right panels) approximations. The inclu-

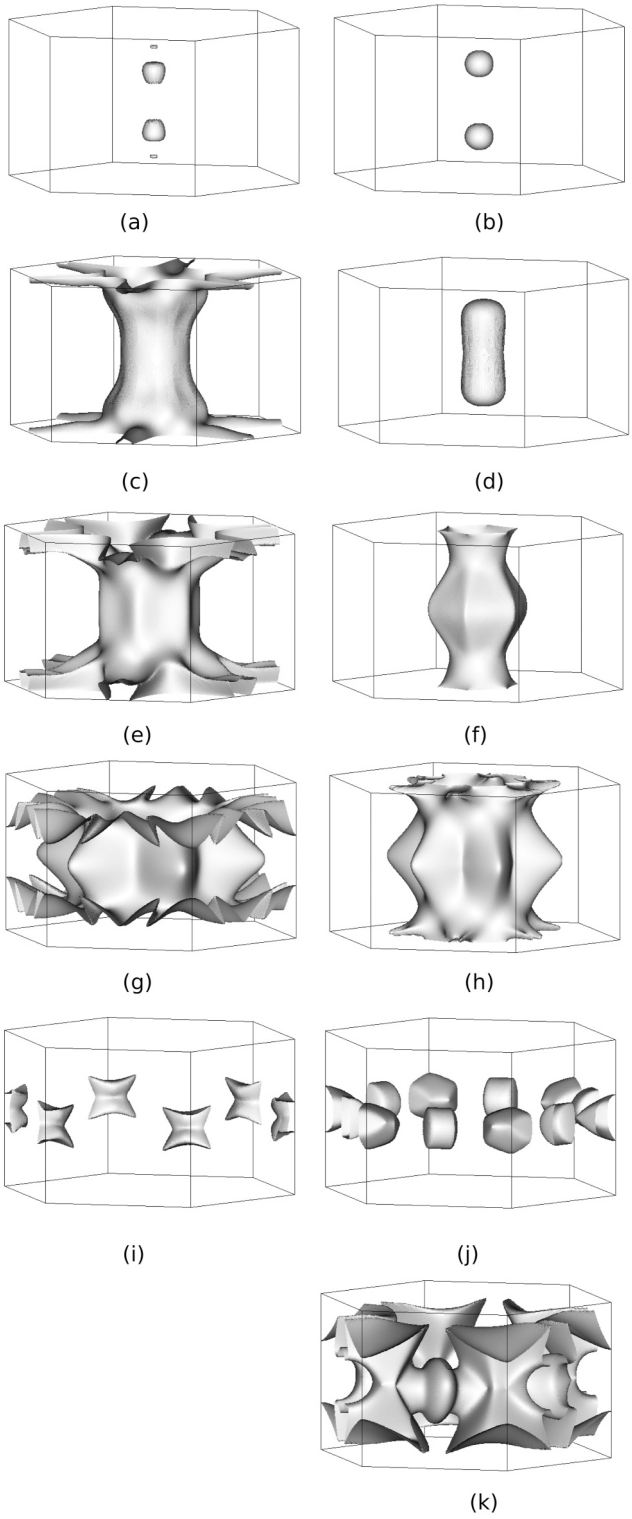

Fig. 7. (Color online) The LSDA+SO (left panels) and the LSDA+SO+*U* (right panels) sheets of MnBi Fermi surface [45].

sion of the SO interaction changes the topology of the FS in MnBi (Fig. 6). Instead of two sheets in the *K* symmetry point in the LSDA calculations we have only one electron FS. Besides, there are four FS cross-sections in the $k_z = 0$ plane in the spin-polarized calculations and three in the LSDA+SO calculations.

There are five sheets of the FS in the LSDA+SO calculations. Almost spherical closed-hole FS centered approximately at a half distance between Γ and *A* symmetry points in Fig. 7(a), has pure Mn 3*d* character. The 23, 24, and 25 hole FSs opened along the Γ – *A* direction with sixfold symmetry in Figs. 7(c), (e), and (g), respectively, are mostly due to Bi 6*p* states with small amounts of Mn 3*d* states mixed in. A closed electron FS centered in the *K* symmetry point in Fig. 7(i) is the mix of Mn 3*d* and Bi 6*p* character.

Inclusion of the Coulomb repulsion increases the size of the 22d hole FS in Fig. 7(b) and reconstruct the 24th and 25th hole FSs in Figs. 7(f) and 7(h)). It produces a new hole FS sheet (see Fig. 7(k)). Dashed black curve in the lower panel of Fig. (5), and an additional closed electron FSs centered in *M* symmetry point (lower panel of Fig. 6).

Figure 8 presents the angular variations of the theoretically calculated dHvA frequencies in MnBi in the LSDA+SO+U approximations for field direction in the $(10\bar{1}0)$, $(11\bar{2}0)$, and (0001) planes [45]. The obtained six different type orbits α, β, γ, δ, ε, and σ belong to the FSs derived by the crossing of the 22nd, 23rd, 24th, 25th, 26th, and 27th energy bands, respectively. The α orbits situated at the almost spherical closed hole FS which centered at a half distance between Γ and *A* symmetry points (Fig. 7(b)). Due to smallness and almost spherical shape of these sheets, the corresponding dHvA frequencies are rather small and have almost constant angle dependence. The β oscillations belong to electron FS around the *K* and *M* points. These orbits split for three separate β_1, β_2, and β_3 orbits. The β_3 oscillations belong to the closed electron FS sheets around the *M* symmetry point. The β_1 and β_2 are at

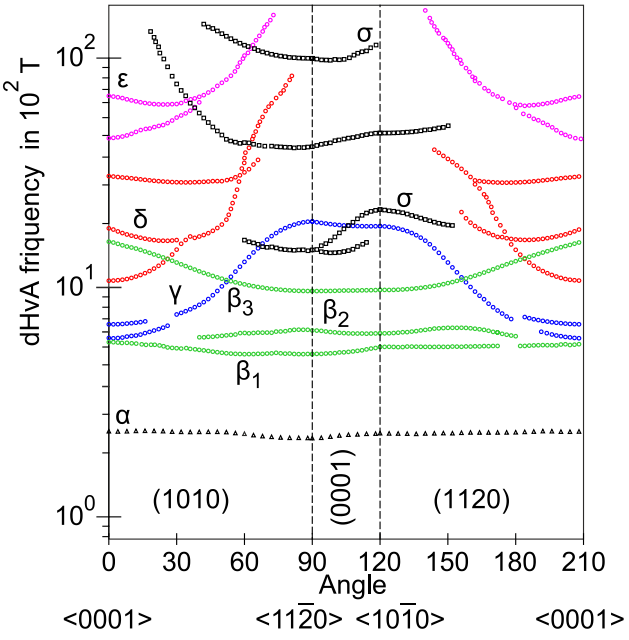

Fig. 8. (Color online) The calculated angular dependence of the dHvA oscillation frequencies in MnBi using LSDA+SO+*U* (*U* = 4 eV) approximation [45].

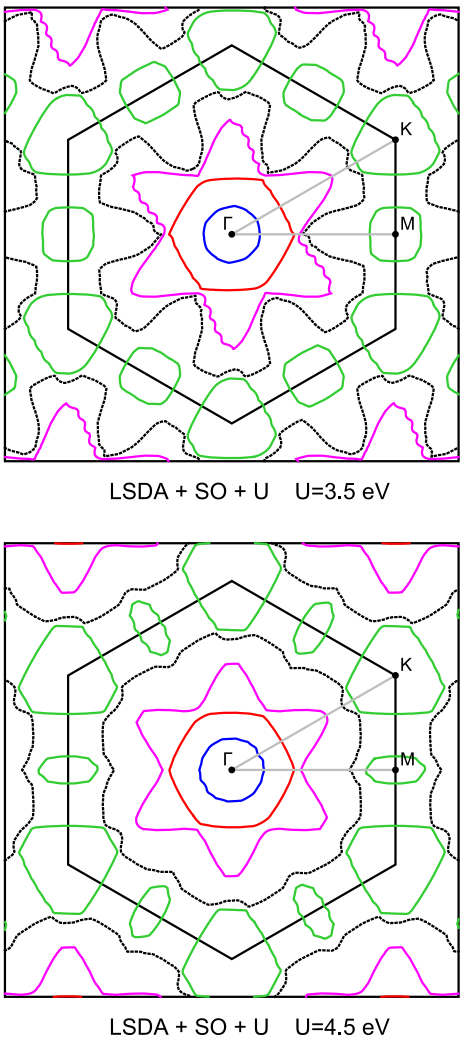

Fig. 9. (Color online) The calculated cross sections of MnBi FS in the plane perpendicular to the z direction $k_z = 0$ using fully relativistic LSDA+SO+U method for $U = 3.5$ eV (upper panel) and $U = 4.5$ eV (lower panel) [45].

the electron FS around the K point (see Fig. 6 lower panel). The γ and δ orbits exist in wide-angle interval at all the three planes. The highest dHvA frequencies were observed for the ε orbits situated at the hole surface derived from the 26th energy band.

The masses for the low-frequency oscillations α range from $-1.0m_0$ to $-0.65m_0$, and the dHvA β orbits on the electron FS sheet around the K symmetry point possess relatively small cyclotron masses from $0.5m_0$ to $0.8m_0$. The δ orbits also have relatively small cyclotron masses of $-0.8m_0$ to $-0.4m_0$ [45]. However, some branches of the δ orbits possess cyclotron masses more than $2m_0$. The masses for the high-frequency oscillations ε are large.

To show how sensitive are the calculations of the FS to the value of Hubbard U, we present in Fig. 9 the calculated cross-sections of MnBi FS for $U = 3.5$ eV and $U = 4.5$ eV [45]. After comparing this figure with Fig. 5 for $U = 4.0$ eV, we can conclude qualitatively that all the three calculations

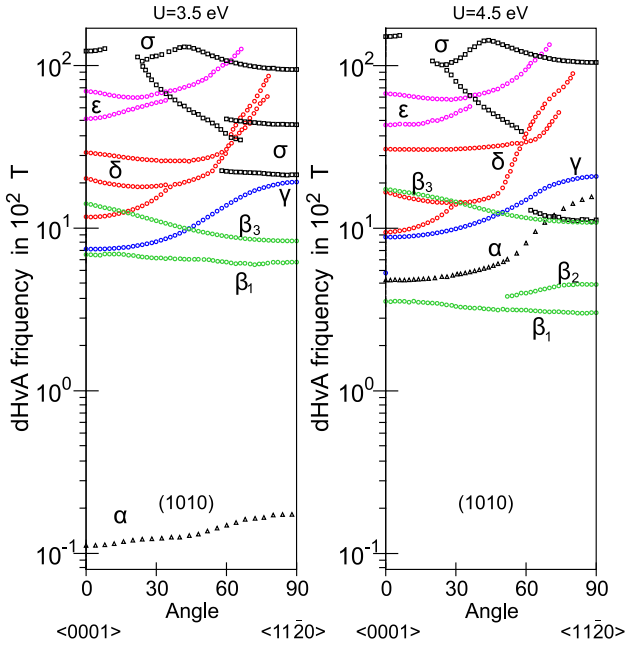

Fig. 10. (Color online) The calculated angular dependence of the dHvA oscillation frequencies in MnBi using LSDA+SO+U approximation for $U = 3.5$ eV (left panel) and $U = 4.5$ eV (right panel) [45].

produce similar FSs with small changes in the size and the shape of some FS sheets. However, the dHvA oscillations are quite sensitive to the value of Hubbard U (see Fig. 10). The frequencies of the α orbits are significantly reduced for $U = 3.5$ eV and increased for $U = 4.5$ eV in comparison with $U = 4.0$ eV calculations. The δ and ε orbits have an opposite U behavior, their frequencies are decreased with the increase of U. On the other hand, the σ and γ orbits are less sensitive to the value of U.

The experimental measurements of the dHvA effect is highly desired, it will answer which value of Hubbard U is realized in MnBi. From the experimental point of view, it would be no problem to measure the dHvA oscillations in MnBi do due to relatively small cyclotron masses for most dHvA orbits. However, a single crystal sample of good quality might be needed.

4.2. Magneto-crystalline anisotropy

It has been established that such unique temperature dependence of the coercivity and MAE in MnBi is determined by the thermal variation of the lattice parameters a and c. In the following section, we explain experimental observations by examining the dependence of calculated total energy and MAE on the lattice geometry. We assume that the finite temperature can be mimicked by the lattice constants corresponding to this temperature. We confirm that spin reorientation arises from a change of sign in MAE, which depends on the lattice constants.

Figure 11 shows the experimentally measured temperature dependence of the lattice constants a and c according to the Refs. 85, 86 together with the magnetization [85]

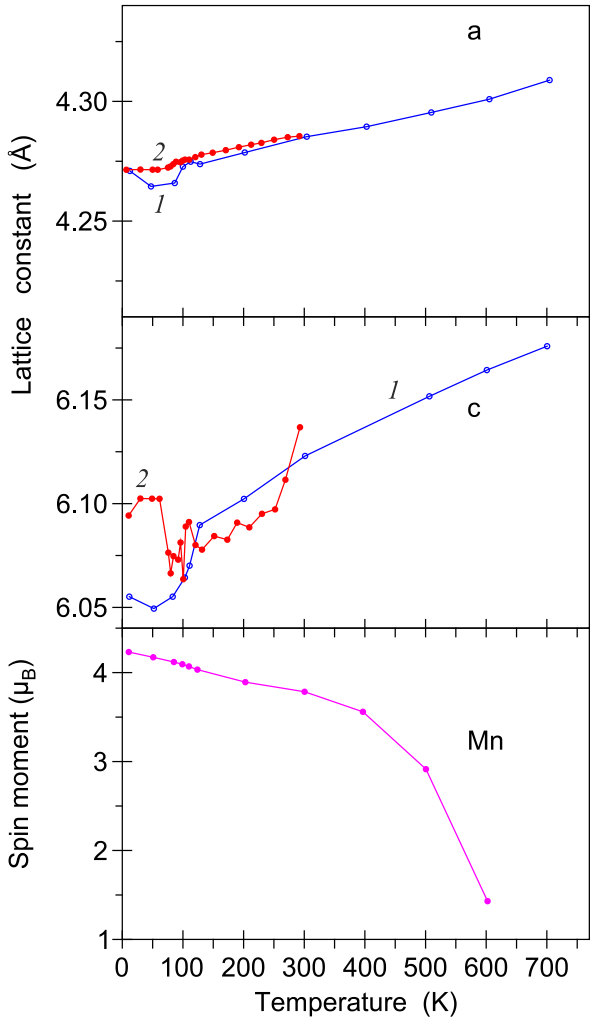

Fig. 11. (Color online) The temperature dependence of the lattice parameters a and c (upper and middle panels, respectively) of MnBi according to the Ref. 85 (blue curve *1*) and Ref. 86 (red curve *2*). The lower panel shows the temperature dependence of magnetization in MnBi [85].

in MnBi. Yang *et al.* [85] measured temperature dependence of the lattice parameters a, and c in a wide temperature range from 10 to 700 K. Koyoma *et al.* [86], on the other hand, used a smaller temperature interval (10–300 K). They did use a very fine temperature mesh in the vicinity of T_{SR}. Both measurements show similar behavior for the lattice constant a, but strongly differ from each other in the temperature behavior of lattice constant c. The results of Yang *et al.* [85] show a rather smooth decrease of parameter c with decreasing of T below T_{SR}. Koyoma *et al.* [86] found a discontinuous behavior of constant c near T_{SR} (Fig. 11).

Figure 12 shows the MAE as a function of the polar angle θ and temperature calculated with the LSDA+SO and the LSDA+SO+U methods [45]. Here the temperature dependence of the lattice constants a and c obtained by Yang *et al.* [85] was used. The LSDA+SO approach gives the value of MAE equal to –2.2 meV/cell at zero temperature. This value is in good agreement with the FPLAPW band structure calculation by Ravindran *et al.* [35] (–2.0 meV/cell). However, both of these values are an order of magnitude larger than the experimental value of –0.13 meV/cell [18,87]. Besides, the LSDA+SO approximation shows that the direction of the easy magnetization is in the basal plane for any value of lattice constant a and axial ratio c/a (meaning the entire temperature range) and, therefore, provides no explanation of the spin-reorientation observed experimentally at the $T_{SR} \sim 90$ K. On the other hand, the LSDA+SO+U approach gives the value of MAE equal to –0.39 meV/cell at zero temperature. This value is already in better agreement with the experiment, but still nearly three times larger than the experimentally estimated value of –0.13 meV/cell [18,87]. Thus the inclusion of the Coulomb correlations provides a correct easy magnetization direction along c axis for the temperatures above T_{SR1} and in the plane below T_{SR} for the experimental parameters a and c.

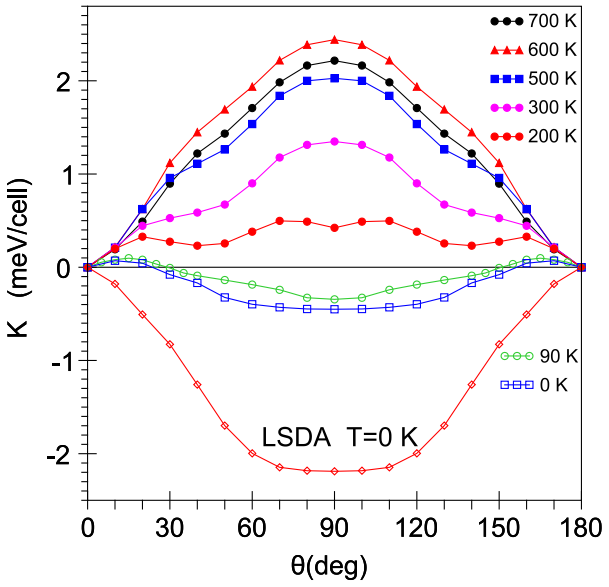

Fig. 12. (Color online) The MAE K as a function of the polar angle θ and temperature in MnBi calculated in the LSDA+SO (open blue squares) and the LSDA+SO+U methods [45]. The used temperature dependence of the lattice constants a and c is from Ref. 85.

Figure 13 presents the theoretically calculated temperature dependence of the MAE in MnBi [45] using the LSDA+SO+U approximation in comparison with the experiment [18]. The theoretical MAE is in a very good agreement with the experiment in the 150 K to 450 K temperature range. Thus, the theoretical calculations confirm the experimental claim [86] that the unusual temperature dependence of MAE is primarily due to a specific lattice thermal expansion. In addition, the theoretical analysis has shown that the increase of uniaxial MAE in this temperature range is related to the increase of uniaxial MAE produced by the anisotropic component of transversal pairwise

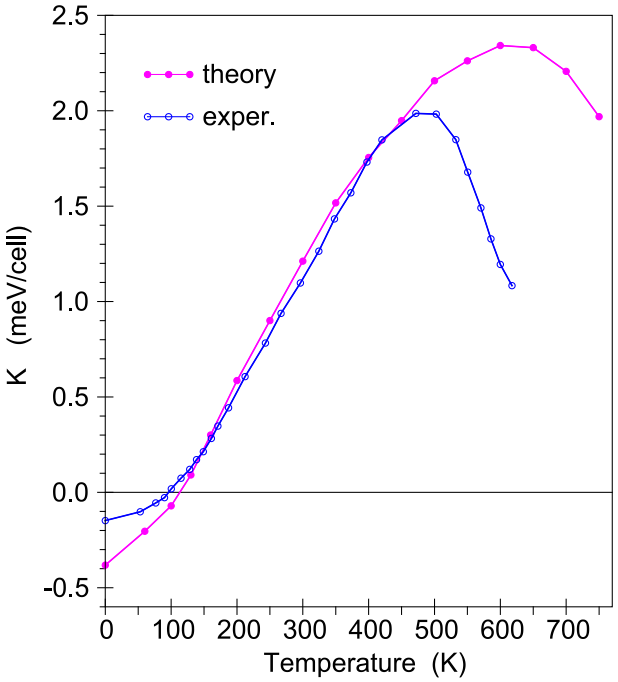

Fig. 13. (Color online) Theoretically calculated temperature dependence of the MAE K in MnBi using the LSDA+SO+U [45] in comparison with the experiment [18].

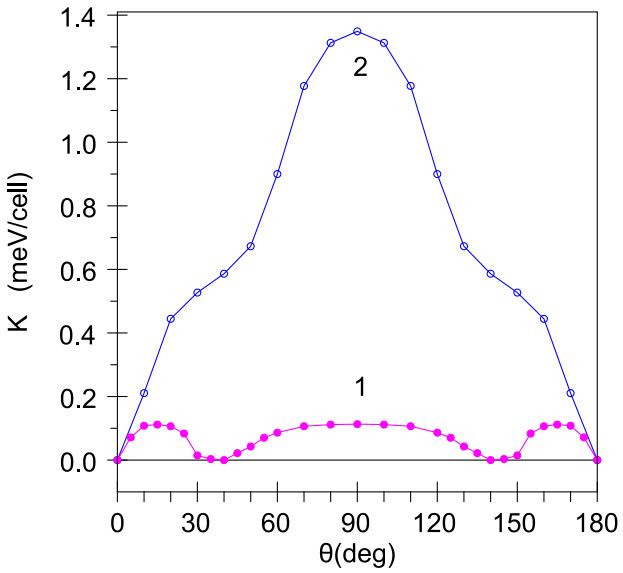

Fig. 14. (Color online) The LSDA+SO+U calculations of the MAE K as a function of the polar angle θ for the lattice constant c = 6.123 Å [45]. This corresponds to the T = 300 K and a = 4.272 Å (curve *1*) and a = 4.283 Å (curve *2*) corresponding to the T = 100 K and 300 K, respectively [85].

interaction between d-states of Mn and p-states of Bi atoms [45].

With the temperature increase above RT, the experimentally measured anisotropy energy increases and reaches its maximum at around 500 K, and then rapidly decreases at higher temperatures. The LSDA+SO+U results show the same temperature behavior. They, however, show higher MAE in the maximum. Besides, the theoretically calculated maximum of the MAE shifts towards higher temperatures (Fig. 13). Such disagreement between the theory and experiment might be due to the magnetic spin disorder effect. The temperature dependence of magnetization in MnBi measured by Yang *et al.* [85] shows a drastic reduction of the magnetization from the 4.25μ_B at 0 K to the 1.43μ_B for 600 K. This presumably due to spin disorder (see lower panel of Fig. 11). Such an effect has not been taken into account in the calculations.

Authors of Ref. 45 found a strong dependence of the MAE on in-plane lattice constant a. Figure 14 shows the MAE as a function of the polar angle θ for the lattice constant c = 6.123 Å. This corresponds to T = 300 K and a = 4.272 Å (curve *1*) and a = 4.283 Å (curve *2*) corresponding to the T = 100 K and 300 K, respectively [85]. Expansion of in-plane lattice constant a by 0.01 Å occurs from 100 K and 300 K increases the MAE by approximately 1.2 meV. Corresponding results for c parameter expansion produce a much smaller result of 0.1 meV (Fig. 14).

To investigate the MAE as a function of the polar angle θ in the vicinity of the spin reorientation phase transition, authors of Ref. 45 fixed the lattice constant a for the spin-reorientation temperature a = 4.274 Å [86] and vary c from c = 6.09 Å to c = 6.14 Å with a step of 0.01 Å (Fig. 15). For the lattice constants c = 6.09 Å, c = 6.10 Å, and c = 6.11 Å (curves *1–3*, respectively), the easy magnetization direction is in the basal plane. There are two local minima in the total energy for the c = 6.12 Å (curve *4*): one

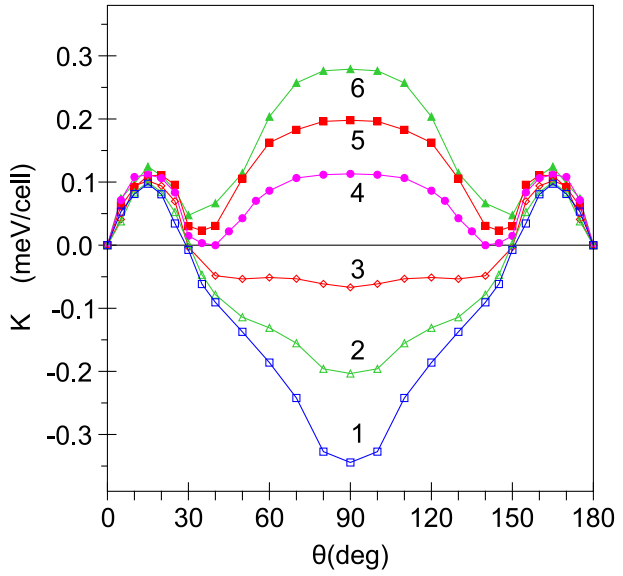

Fig. 15. (Color online) The LSDA+SO+U calculations of the MAE K as a function of the polar angle θ for the lattice constant a = 4.274 Å [45]. This corresponds to the spin-reorientation (T_{SR} = 90 K) [86] and c = 6.09 Å (curve *1*), c = 6.10 Å (curve *2*), c = 6.11 Å (curve *3*), c = 6.12 Å (curve *4*), c = 6.13 Å (curve *5*), and c = 6.14 Å (curve *6*).

along the c direction and at the $\theta \sim 41°$ with a barrier in between. The last angle is close to the experimentally measured $\theta_{exp} = 37°$ at $T_{SR} = 90$ K where the magnetization flops into the ab basal plane [17] (see Fig. 2). For larger values of the lattice constant c, the easy magnetization direction is along the c direction in agreement with experimental observation. We would like to point out that the results presented in Fig. 15 have to be considered only as qualitative ones because by fixing the constant a and varying c, the c/a has altered the an overall volume per unit cell.

The results shown in Fig. 15 lead to some interesting conclusions. The angular dependence of the total energy demonstrates the presence of a "double-well" potential. This fact leads to a hysteresis phenomenon as a function of temperature. For instance, one can expect a non-smooth dependence of the magnetization direction change with a "sudden" switch of easy direction at different temperatures depending on whether a cooling or heating process is being used. This qualitatively explains the non-analytical dependence of easy axes observed in Ref. 17 (see Fig. 2). The total energy shows a highly non-trivial angular dependence with several minima. This leads to a hysteresis behavior of magnetization as a function of temperature.

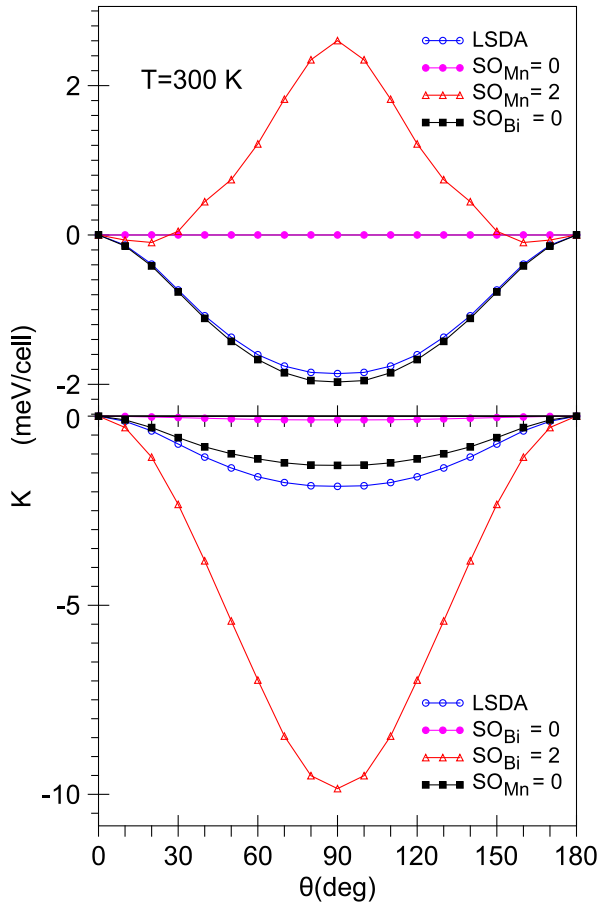

Fig. 16. (Color online) The effect of scaling of the exchange splitting (upper panel) and value of SO constant (lower panel) on either Mn or Bi atoms on the MAE K in MnBi [45] (see the text).

This, in turn, creates a condition for a non-continuous spin reorientation transition that can be considered as a planar to the uniaxial anisotropy phase transition.

We can conclude that the increase of MAE with temperature presented in Fig. 13 is mostly due to changing the in-plane lattice constant a.

We examine the dependence of the MAE on the exchange splitting and the SO interaction. The exchange splitting and SO coupling are studied by scaling the corresponding terms in the Hamiltonian artificially with a constant prefactor. This scaling can be atom dependent, i.e., within each atomic sphere. The outcomes of such constraining calculations for the MAE in MnBi are shown in Fig. 16. In the upper panel, the importance of the exchange splitting is illustrated. When the exchange splitting on Bi is set to zero, the MAE is barely modified. But when we performed such operation on Mn atom, the MAE totally vanishes. Furthermore, an enhancement of the exchange splitting on Mn by a factor of 2.0 (red open triangles) leads to a correct easy magnetization along the z direction.

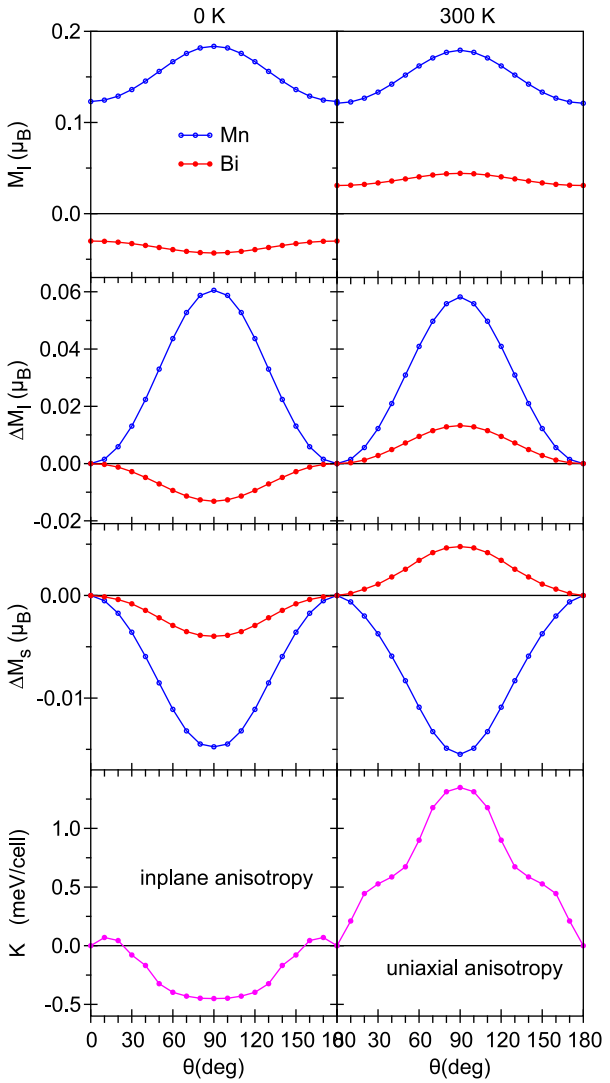

Fig. 17. (Color online) The MAE, M_l, OMA (ΔM_l) and SMA (ΔM_s) for $T = 0$ K (left panel) and $T = 300$ K (right panel) [45].

The lower panel of Fig. 16 shows the dependence on the SO coupling. If SO coupling on Mn set to zero, the MAE does not change significantly (full black squares). On the other hand, when the SO coupling on Bi is zero, the MAE almost disappears (magenta full circles). The scaling of the SO coupling of Bi by a factor of 2.0 leads to an increase of the MAE by a factor of 5 confirming a dominant contribution of the SO interaction at the Bi site to the large value of MAE in this compound.

It is customary to relate the MAE with the anisotropy of M_l (OMA) [88–90]. Figure 17 presents the MAE, M_l, OMA, and the anisotropy of M_s (SMA) for $T = 0$ K and $T = 300$ K. The M_l, OMA and SMA are larger at the Mn site than at the Bi one. The OMA is four times larger than the SMA for both sites. The Bi M_l change the sign through spin-reorientation transition, therefore the inversion of the MAE through the spin-reorientation transition is directly correlated with OMA at the Bi site.

The MAE is proportional to the OMA through expression $K \sim \frac{1}{4}\lambda\Delta M_l$ [88–90], where λ is the SO parameter. The SO constant $\lambda = 0.041$ eV for 3*d* Mn ion, but $\lambda \sim 0.85$ eV for Bi [91]. Therefore, the major contribution to the MAE is due to the OMA at the Bi site. Although the SMA is smaller than OMA for both sites, one would expect some contribution to the MAE from the SMA.

5. Excited-state properties

5.1. Magneto-optical properties

In this section we provide a theoretical explanation of the MO properties of MnBi.

The experimental Kerr spectra as well as the calculated ones are shown in Fig. 18. The Kerr rotation is denoted by θ_K and the Kerr ellipticity by ε_K. First-principles LSDA theory predicts a very large Kerr rotation in MnBi of about −2° at 1.8 eV. This is even larger than the measured peak value of −1.6° [25]. The experiment shows a second maximum in the Kerr angle at 3.4 eV. Here the LSDA calculations give only a shoulder. The reason for such disagreement is the underestimation of the M_s in the LSDA [45]. The M_s at the Mn site is equal to $3.572\mu_B$ in the LSDA. However, the experimental value at low temperature is equal to $4.25\mu_B$ [85]. In Fig. 18, we present the calculated Kerr spectra in the LSDA+SO+*U* (red full lines) and the LSDA+SO calculations with an artificially increased exchange splitting on the Mn site by 1.5 times (black dotted curves). In both latter calculations the M_s is quite close to the experimental value ($4.234\mu_B$ and $4.257\mu_B$ for the LSDA+SO+*U* and the LSDA+SO with increased spin splitting, respectively). Both spectra have similar shapes with much better reproduction of the second maximum in the Kerr angle at 3.4 eV. Another feature of the experimental Kerr rotation is that it exhibits a sign reversal at 0.9 eV. This sign reversal is actually also given by the LSDA+SO method, but for a smaller energy. The LSDA+SO+*U* method

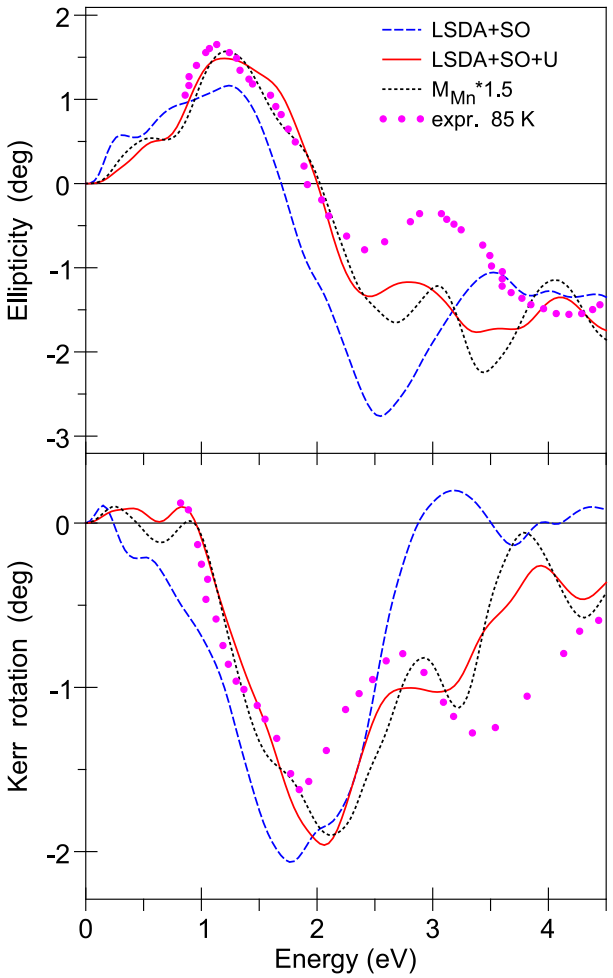

Fig. 18. (Color online) Calculated in the LSDA+SO (blue dashed lines) and LSDA+SO+*U* (red full lines) approximations polar Kerr rotation (θ_K) and Kerr ellipticity (ε_K) spectra of MnBi [45] in comparison with the experimental measurements from Ref. 25. M_{Mn}*1.5 denotes an exchange splitting of 150% of the first-principles value.

and the LSDA+SO one with increased spin splitting perfectly reproduces the energy of a sign reversal at 0.9 eV. The LSDA+SO+*U* approximation also reproduces better the observed shape of the Kerr ellipticity and a sign reversal at around 2 eV (see upper panel of Fig. 18).

The Kerr spectra depend on the MO conductivity spectra in an entangled way. Therefore, it is difficult to assign features in the Kerr spectra to particular band transitions. The absorptive parts of the optical conductivity σ_{1sxx} and σ_{2sxy} however, relate directly to the interband optical transitions, and therefore provide more physical insight [57,92]. The calculated absorptive part of off-diagonal optical conductivity σ_{2xy} for MnBi is shown in Fig. 19. The main peak in the Kerr rotation of MnBi is due to the maximum in the σ_{2xy} at 1.8 eV. The second fine structure in MnBi Kerr spectrum at 3.4 eV corresponds to the high energy peak in the σ_{2xy} at the same energy. The LSDA+SO calcu-

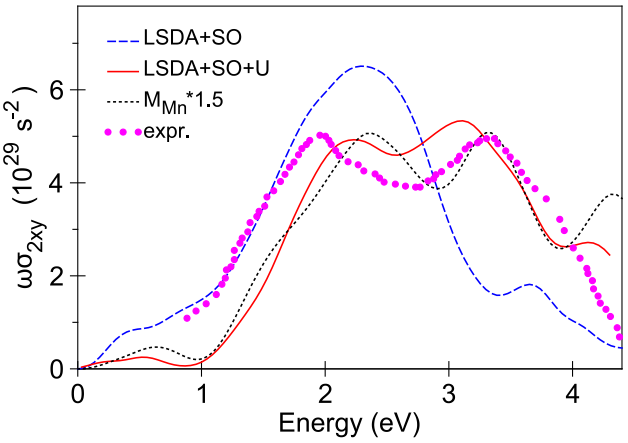

Fig. 19. (Color online) Calculated in the LSDA+SO (blue dashed lines) and LSDA+SO+U (red full lines) approximations off-diagonal component (σ_{2xy}) of the conductivity tensor for MnBi [45] in comparison with the experimental measurements in MnBi from Ref. 25. M_{Mn}*1.5 denotes an exchange splitting of 150% of the first-principles value.

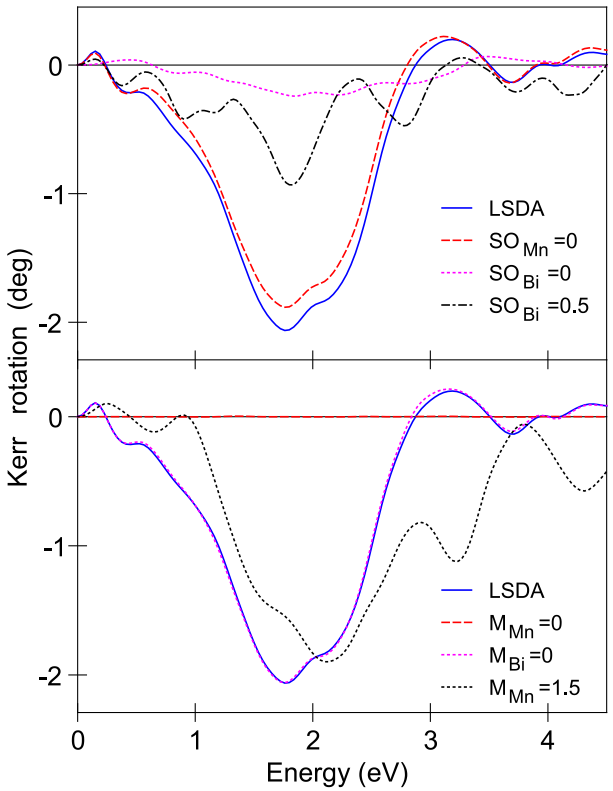

Fig. 20. (Color online) The effect of scaling of the exchange splitting (upper panel) and value of SO constant (lower panel) on either Mn or Bi atoms on the MO Kerr spectra in MnBi (see the text) [45].

lations strongly underestimate the intensity of the second high energy peak in the σ_{2xy}. As a result, the LSDA+SO fails to correctly describe the second negative peak in the Kerr rotation at 3.4 eV. On the other hand, the LSDA+SO+U and the LSDA+SO with increased spin splitting quite well reproduce the intensity of the second high energy peak in the σ_{2xy} spectrum and therefore better describes the 3.4 eV peak in the Kerr rotation.

We can conclude that the main reason for the failure of LDSA to describe the MO properties in MnBi is the significant underestimation of spin magnetic moment on the Mn atom. Two very different techniques (the LSDA+U method and the application of external magnetic field on the Mn atom) produced similar spin moment enhancement and consequently better MO values.

It is important to identify the origin of the large Kerr effect in MnBi. To this end, authors of Ref. 45 examine the dependence of the MO spectra on the exchange splitting and the SO interaction. The exchange splitting and the SO coupling were studied by scaling the corresponding terms in the Hamiltonian artificially with a constant prefactor. These modifications can be done within each atomic sphere independently so that we can investigate the separate effects of these quantities on Mn and Bi. The outcomes of these model calculations for the Kerr rotation of MnBi are shown in Fig. 20. In the lower panel, the importance of the exchange splitting is illustrated. When the exchange splitting on Bi is set to zero, the Kerr rotation remains as it is. But when we do the same for the exchange splitting on Mn, the Kerr rotation totally vanishes. This implies that the exchange splitting due to Mn is crucial for the sizable Kerr rotation, but that of Bi is not important. Furthermore, an enhancement of the exchange splitting on Mn by a factor of 1.5 (dotted line) leads to a much larger peak in the Kerr rotation at 3.4 eV. The upper panel of Fig. 20 shows the dependence on the SO coupling. If we set the SO coupling on Mn to zero, the Kerr rotation does not change very much (dashed red line). On the other hand, when the SO coupling on Bi is zero, the Kerr rotation almost disappears (dotted magenta line). Thus, the SO coupling of Bi is equally responsible for the large Kerr rotation as is the exchange splitting of Mn. An intermediate scaling of the SO coupling of Bi by a factor of 0.5 leads to an approximately half as large Kerr angle, thereby illustrating the almost linear dependence of the Kerr effect on the SO interaction of Bi in this compound.

5.2. X-ray magnetic circular dichroism

Motivated by the developing interest in obtaining element-specific magnetic moment information provided by XMCD measurements authors of Ref. 45 calculate the XAS and XMCD spectra of MnBi at the Mn K, and $L_{2,3}$ and at the Bi $M_{2,3}$, $M_{4,5}$, $N_{2,3}$, $N_{4,5}$, $N_{6,7}$, and $O_{2,3}$ edges.

Figure 21(a) shows the theoretically calculated x-ray absorption spectra at the Mn K edge in MnBi with the electric field vector of the x rays both parallel (dashed red curve) and perpendicular (full blue curve) to the c axis. The associated XLD signal (obtained by taking the difference of the XA spectra for the two polarizations) is given in the pa-

nel (b) of Fig. 21. Fig. 21(c) shows the theoretically calculated XMCD in terms of the difference in absorption $\Delta\mu_K = \mu_K^+ - \mu_K^-$ for left and right circularly polarized radiation in MnBi. After comparing the panels (b) and (c), we can conclude that the XMCD signal is almost one order of magnitude smaller than the corresponding XLD signal. Also, the spectra have major peaks in different energy intervals. Major peaks in the XMCD spectrum are mostly located in the 0 to 15 eV energy interval. However, the XLD spectrum possesses the major peaks above 15 eV.

Because dipole allowed transitions dominate the absorption spectrum for unpolarized radiation, the absorption coefficient $\mu_K^0(E)$ reflects primarily the DOS of unoccupied $4p$-like states $N_p(E)$ of Mn above the Fermi level. Due to the energy-dependent radial matrix element for the $1s \to 4p$, there is no strict one-to-one correspondence between $\mu_K(E)$ and $N_p(E)$. The exchange splitting of the initial $1s$-core state is extremely small and therefore only the exchange and SO splitting of the final $4p$-states is responsible for the observed dichroism at the K-edge. For this reason, the dichroism is found to be quite small (lower panel of Fig. 21).

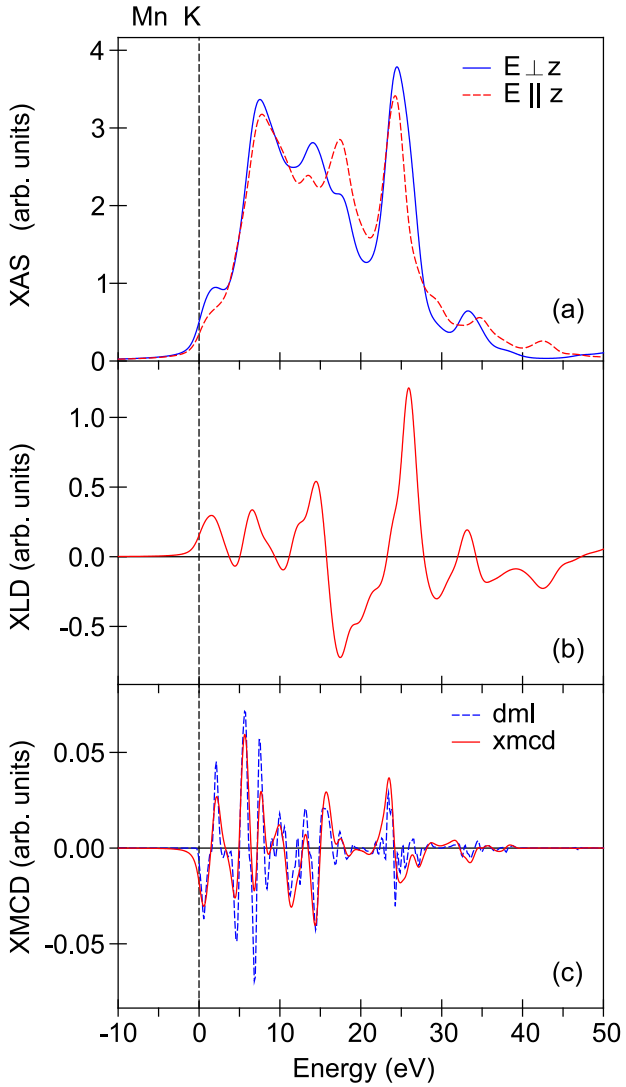

Fig. 21. (Color online) (a) the theoretically calculated x-ray absorption spectra of MnBi at the Mn K edge with the electric field vector of the x rays parallel (red dashed curve) and perpendicular (blue full curve) to the z-axis [45]; (b) theoretically calculated XLD spectra at the Mn K edge [45]; (c) the theoretically calculated XMCD spectrum at the Mn K edge (red full curve) and dm_l function (blue dashed curve) [45]. The calculations have been done using the LSDA+SO+U approach.

To illustrate the influence of SO interaction on the final states involved in the transitions, let us introduce a site-dependent function $dm_{tl}(E)$ given by [93]:

$$dm_{tl}(E) = \sum_{m_j}\sum_{n\mathbf{k}} \left\langle \Psi_{tl}^{n\mathbf{k}} \mid \hat{l}_z \mid \Psi_{jm_j} \right\rangle \delta(E - E_{n\mathbf{k}}), \quad (8)$$

where $\hat{l}_z$ is the z projection of the angular momentum operator, $E_{n\mathbf{k}}$ and $\Psi_{tl}^{n\mathbf{k}}$ are the energy of the nth band and the part of the corresponding LMTO wave function formed by the states with the angular momentum l inside the atomic sphere centered at the site t, respectively. In analogy to the l-projected density of states, $dm_{tl}(E)$ can be referred to as site- and l-projected density of the expectation value of $\hat{l}_z$.

The $4p-3d$ hybridization and the SO interaction in the $4p$ states play a crucial role in the Mn K edge dichroism. As seen in Fig. 21(c), the K XMCD spectrum and $dm_{tl}(E)$ functions are closely related to one another and give a rather simple and straightforward interpretation of the XMCD spectra at the K edge.

Because of the dipole selection rules and apart from the $4s_{1/2}$-states (which have a small contribution to the XAS due to relatively small $2p \to 4s$ matrix elements [57]), only $3d_{3/2}$-states occur as final states for L_2 XAS for unpolarized radiation. Whereas for L_3 XAS the $3d_{5/2}$-states also contribute. Although the $2p_{3/2} \to 3d_{3/2}$ radial matrix elements are only slightly smaller than elements for the $2p_{3/2} \to 3d_{5/2}$ transitions the angular matrix elements strongly suppress the $2p_{3/2} \to 3d_{3/2}$ contribution. Therefore in neglecting the energy dependence of the radial matrix elements, the L_2- and the L_3-spectrum can be viewed as a direct mapping of the DOS curve for $3d_{3/2}$- and $3d_{5/2}$-character, respectively.

In contrast to the K edge, the dichroism at the L_2 and L_3 edges is also influenced by the SO coupling of the initial $2p$-core states. This gives rise to a very pronounced dichroism in comparison with the dichroism at the K edge. Figure 22 shows the theoretically calculated Mn $L_{2,3}$ XMCD spectra in MnBi. The XMCD spectra at the $L_{2,3}$-edges are mostly determined by the strength of the SO coupling of the initial $2p$-core states and spin-polarization of the final empty $d_{3/2,5/2}$ states. The exchange splitting of the $2p$-core states as well as the SO coupling of the $3d$-valence states are of minor importance for the XMCD at the $L_{2,3}$-edge of $3d$-transition metals [57].

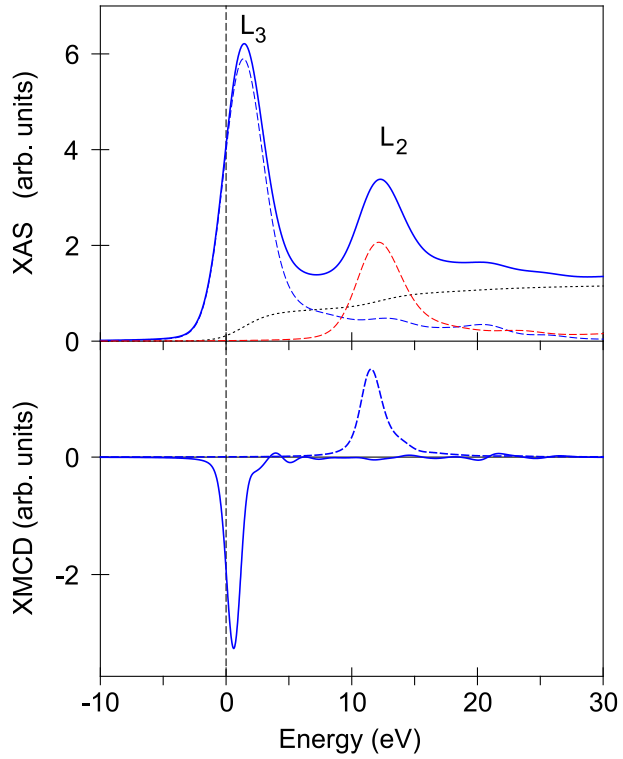

Fig. 22. (Color online) X-ray absorption (top panel) and XMCD spectra (lower panel) at the Mn $L_{2,3}$ edges calculated using the LSDA+SO+U [45].

6. MnBi: A potential candidate for rare-earth free permanent magnets

Permanent magnets (PMs) are critical components for electric motors and power generators. Key properties of permanent magnets, especially coercivity and remanent magnetization, are strongly dependent on microstructure. The widely used PMs for the traction motor in electric vehicles and the power generator in wind turbines contain rare earth elements Nd and Dy due to their high maximum energy product. Due to the high supply risk of RE elements such as Dy and Nd, these elements are listed as critical materials by the international institutes. Compared to rare earth PMs, non-rare earth (non-RE) PMs typically have lower maximum energy products, however, given their small supply risks and low cost, they are being intensively investigated for less-demanding applications. The general goal for the development of non-RE PMs is to fill in the gap between the most cost-effective but low performing hard ferrite magnet and the most expensive but high performing RE PMs [94]. In the past decade, great progress has been made toward improving the physical properties of non-RE PMs. Several new candidate materials systems were investigated, and some have shown realistic potential for replacing RE PMs for some applications. One of them is LTP-MnBi compound.

$Nd_2Fe_{14}B$ (NdFeB) magnets are widely used for conversion between electricity and mechanical energy. Unfortunately, the magnetic properties of NdFeB is strongly temperature-dependent [94]. The $(BH)_{max}$ of the NdFeB magnet falls sharply once temperature exceeds 373 K (as shown in Fig. 23). Permanent magnet motors and generators using NdFeB magnets must consider some form of a cooling mechanism to dissipate the heat generated by eddy current and friction. Better thermal stability (up to 50% increase of $(BH)_{max}$ at 473 K) can be achieved by adding Pr and Dy [95].

The best known hard magnetic materials have usually a lower saturation polarization J_s than many soft magnetic materials. They are chemically very reactive and also expensive on account of a substantial content of a rare earth. It is possible to make permanent magnets of composite materials consisting of two suitably dispersed ferromagnetic and mutually exchange-coupled phases, one of which is hard magnetic to provide high anisotropy and high coercive field, while the other may be soft magnetic just providing a high saturation magnetization [96]. A general theoretical treatment of such systems shows that one may expect besides a high-energy product $(BH)_{max}$ two uniquely characteristic features, a reversible demagnetization curve ("exchange-spring") and, in certain cases, an unusually high isotropic remanence ratio B_r / J_s while the required volume fraction of the hard phase may be very low, of the order 10% [96]. The technological realization of such materials has to be based on the principle that all phases involved must emerge from a common metastable matrix phase to be crystallographically coherent and consequently magnetically exchange-coupled. Theoretical work suggests that

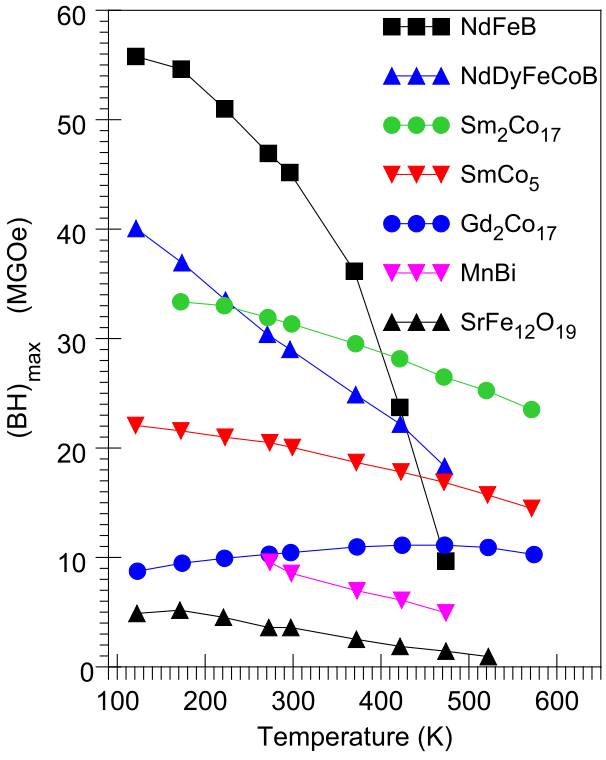

Fig. 23. Temperature dependence of $(BH)_{max}$ most commercial permanent magnets. (Data extracted from Ref. 94).

energy products could significantly surpass those provided by conventional uncoupled magnetic materials [97], and experiments have verified that energy products are indeed increased [98–101]. However, to date, the technical magnetic properties of the resultant products have not come close to their theoretical promise due to unresolved issues of phase purity, uniformity, and crystallographic alignment.

Although, the low-temperature phase of MnBi also exhibits many intriguing properties, described partly in the first part of the Review, the fabrication of ferromagnetic MnBi remains challenging, since the reaction between Mn and Bi is peritectic due to the large difference in melting temperature between Mn (1519 K) and Bi (544 K). Besides, Mn easily reacts with oxygen, causing decomposition of MnBi [94]. In addition, according to the phase diagram (Fig. 1), MnBi exists in several closely related phases, among which only the LTP is ferromagnetic.

MnBi was first investigated as a permanent magnet by Adams *et al.* in 1952 [102]. The permanent magnet was prepared by hot pressing finely pulverized MnBi in the presence of a strong magnetic field to facilitate particle alignment. The MnBi magnet possessed a maximum energy product of $(BH)_{max} = 4.3$ MG·Oe, $B_r = 4.3$ kG and $H_c = 3.4$ kOe. Fifty years later, Yang *et al.* re-investigated the subject and improved the room temperature $(BH)_{max}$ to 7.7 MG·Oe [103]. The improvement is attributed to the purification process yielding fewer impurities. The significance of Yang's work is that it showed the importance and difficulty of obtaining a pure MnBi phase. The peritectic reaction between Mn and Bi dictates that regardless of the starting stock composition, the conventional casting process will always result in Mn precipitating out from the MnBi liquid. The diffusion of Mn or Bi to MnBi is slow, which indicates that low-temperature sintering will cost a long time to complete, and it is likely the reaction is only partly complete, leaving behind Mn and Bi as impurities. Historically, the alloy was obtained by sintering Mn and Bi powders at high temperatures. Such a process will yield 60% pure MnBi phases. Magnetic purification was applied to filter the magnetic MnBi phase from the nonmagnetic impurities. However, the purification process will not result in near 100% pure phase because impurities are not always physically separated from the MnBi phase. For example, if the Bi or Mn particles are intimately attached to a MnBi particle, applying the magnetic field will not help separate them. To date, the best record is about 90% pure. Further improvement using the conventional method is presumed to be difficult.

Recently, Li *et al.* [104] show that Ar^+-ion beam bombardment resulted in a 200% increase in the saturation magnetization of the annealed MnBi thin film. This advancement was attributed to the enhanced interdiffusion and reaction of Mn and Bi in the ion-beam-bombarded thin films. This work provides an effective approach for the fabrication of high-quality MnBi thin films.

The α-MnBi based bulk magnet may be commercialized if its energy product exceeds 10 MG·Oe at room temperature. The current state of the art result is close to this target. The approach to push the current 8.7 MG·Oe to 10 MG·Oe is through a novel synthesis approach that can yield 99% pure α-MnBi powder with < 5 μm particle size and through a large scale warm-iso-press system that can densify the aligned compact to over 96% density [94].

6.1. Morphology and fabrication of MnBi

After decades of scientific research, MnBi has emerged as one of the rare-earth-free permanent magnets. As a promising alternative to rare-earth magnets (such as NdFeB magnets), MnBi possesses great magnetocrystalline anisotropy. One of the key features that make MnBi a unique permanent magnet is its positive temperature coefficient of coercivity. In other words, unlike the regular tendency, the coercivity of MnBi increases with increasing temperature. A broad bifurcation shows that MnBi permanent magnets exist in three different forms-bulk, thin films, and nanoparticles. The existence of MnBi in each of these forms and their magnetic properties are majorly dependent on the synthetic methods. Despite many reported scientific works, there are still efforts being made to reach the theoretical value of the energy product of the MnBi, which is around 18 MG·Oe [46].

a. Bulk samples. That small particles of MnBi would behave as elementary magnets was noted by many observers, notably by Frenkel and Dorfman [105], Gottschalk [106], and Dean and Davis [107]. This phenomenon was quantitatively examined by Néel [108], Stoner and Wohlfarth [109], and Kittel [110,111], who derived expressions for the evaluation of the various energies involved. They showed that the effective internal energy of the small particles will be high if (1) the magneto-crystalline anisotropy is high, (2) the particle is elongated, or (3) a severe strain is present in an anisotropic manner. The applied external field necessary to overcome this internal energy is called the coercive force H_c.

The roadmap for developing a MnBi based exchange-coupled magnet starts with preparing high purity MnBi compound in large quantities. Synthesizing MnBi is a challenge. As shown by the Mn–Bi phase diagram Fig. 2, the melting temperatures of Mn and Bi are 1519 K (1246 °C) and 544 K (271 °C), respectively. A rather drastic peritectic reaction exists over wide temperature and composition ranges, therefore, it is very difficult to prepare the single-phase compound using conventional methods. So far, many methods have been tried to avoid the segregation. Several methods have been utilized in preparation of high purity MnBi single phase, including arc-melting, sintering, and melt-spin rapid solidification [1,112–115]. Among them, only rapid solidification was able to consistently produce over 90% pure MnBi single phase. However, a conventional method such as casting followed by heat treatment is

much preferred because of its compatibility with current industrial practice. A recent result by Rao *et al.* shows that the conventional cast-anneal method has the potential to achieve 90% single-phase material [116,117]. The Mn–Bi phase diagram shows that in addition to the peritectic reaction, there is a eutectic reaction at 535 K (262 °C), L ↔ Bi + MnBi. This reaction limits the maximum temperature to which the material can be exposed. While this eutectic temperature is about 62 K higher than the desired operating temperature of 473 K (200 °C), it is rather low for a typical bulk magnet fabrication method such as sintering and hot pressing. In practice, the feedstock powder always contains several percent of Bi metal as the result of the peritectic reaction. Once the fabrication temperature exceeds the eutectic temperature at 535 K, Bi and part of the MnBi will transform to Bi rich liquid. Any trace amounts of oxygen may react with the Mn atoms in the liquid resulting in MnO formation. Once MnO is formed, it cannot be reduced even in the hydrogen environment at a temperature < 535 K. Excessive Bi will be left behind, causing dissolution of even more MnBi. A thorough understanding of MnBi thermal stability is critical for developing a bulk magnet fabrication method as well as determining the maximum and peak operating temperatures.

Gui *et al.* [118] show that the MnBi compound is sensitive to oxygen and temperature. Oxygen is the driving force for MnBi decomposition when subjected to a temperature higher than 473 K. Once decomposed, the Mn reacts with oxygen forming MnO, causing irreversible loss of magnetic properties. On the other hand, if the fabrication temperature is limited to 473 K and below, the MnBi is stable. Furthermore, if the fabrication process has tight control of oxygen, the fabrication temperature may be increased by a few tens of degrees. Therefore, there is a small thermal-mechanical window allowing a bulk MnBi magnet to be fabricated and the resulting magnet is stable up to 473 K (200 °C).

Another way to prepare homogenous MnBi alloys is by using melt-spinning, and LTP MnBi can be obtained with subsequent annealing. Guo *et al.* [115] have prepared high purity LTP MnBi using this method, but the H_c is only 0.2 T at room temperature. Sara *et al.* [119] have used a grinding method to increase the H_c, but the saturation magnetization decreased severely after grind due to the impurity phase. Up to now, no single-phase MnBi with high H_c has been made by melt-spinning. Yoshida *et al.* 112] have reported obtaining MnBi of about 90 wt% by zone-arc-melting under He atmosphere. Yang *et al.* [1] obtained 90 wt% LTP MnBi by sintering Mn and Bi powders and subsequent magnetic purification. Yang *et al.* [120] were prepared nanocrystalline LTP MnBi by melt-spinning and subsequently annealing. It was found the amorphous MnBi ribbons could transform into low-temperature phase by heat treatment in a temperature range of 533–593 K. The coercivity of MnBi was greatly improved by porphyrization, and exhibited a positive temperature coefficient. The maximum energy product $BH_{\max}$ of the anisotropic bonded magnet is 7.1 MG·Oe (56 kJ/m^3) and 4.0 MG·Oe (32 kJ/m^3) at room temperature and 400 K. Zhang *et al.* [121] prepared Mn_xBi_{100-x} (x = 48, 50, 55, and 60) alloys by the induction melting technique, and subjected to melt spinning and subsequent ball milling. X-ray diffraction (XRD) shows that the as-milled powders were mainly composed of LTP MnBi. Increasing melt spinning speed and reducing annealing treatment time can able to restrain the segregation of Mn from MnBi liquid during the peritectic reaction, which increases the LTP MnBi content. High energy ball milling results in the coercivity increase of MnBi powders. With increasing milling time, the coercivity increases initially and then decreases gradually. After ball milling for 4 h, the coercivity of the Mn_xBi_{100-x} powders is 11.4 kOe for x = 48 and 14.8 kOe for x = 55. To date, how to produce pure LTP MnBi remains a big problem for basic science and application.

The melt-spinning process can produce MnBi alloys with accurate composition control. The rapid cooling in the order of 104–107 °C/s can freeze the composition of the starting stock in a liquid state, effectively avoiding the liquid MnBi phase. However, the obtained phase is a single amorphous phase. Following this with an annealing step at 300°C is required to obtain the desired LTP MnBi phase and to avoid the Mn segregation problem. Guo *et al.* have reported that 95% pure MnBi was achieved by rapid solidification, followed by thermal annealing [113]. X-ray diffraction shows that the melt-spun ribbons are amorphous. This surprising result may indicate that the atomic size mismatch may be more important for glass formation than the presence of deep eutectics. The crystallization and transformation of the as-quenched ribbons involve complex processes. The amorphous phase crystallizes first into Bi, Mn_3Bi, and ferrimagnetic MnBi. The formation of LTP MnBi immediately follows the eutectic melting of these phases at 540 K. The amount of Bi present with MnBi (LTP) is less than 5 wt%. Further improvement in the removal of these impurities is expected to be non-trivial.

b. Single crystals. Some authors were able to grow the MnBi monocrystals. Yim and Stofko [122] obtained single crystals of Bi containing ordered MnBi filaments (4% by volume) by a zone-melting technique in the presence of a longitudinal magnetic field. Metallographic and x-ray examinations showed that the long axis of the MnBi needles (4μ in diameter and 200μ long) was aligned along the preferred growth direction, which is perpendicular to the trigonal axis of the single crystalline Bi matrix. The long axis of the needles is the *c* axis of MnBi, the direction of easy magnetization. These needles rendered the eutectic Bi-MnBi crystal ferromagnetic with a strong magnetic anisotropy, as revealed by magnetic moment measurements.

MnBi single crystals were grown by pulling with a seed from a bismuth-rich melt [6,123]. By varying the amount

of excess Bi, the growth could be performed at a temperature in either the low-temperature phase region (below 355 °C) or high-temperature phase region of the compound. The effects of pulling rate and seed orientation on Bi inclusions in the grown crystals were investigated. It was established that at a pulling rate of 0.5 cm per day, Bi inclusions can be minimized by pulling with the crystallographic *c*-axis of the seed normal to the surface of the melt. By changing the growth temperature and Mn concentration in the melt, the effects of phase transformation on the degree of crystallinity and orientation of the crystals grown by this method were investigated. Based on the results of the crystal growth from Bi rich solutions and metallographic analysis of heat-treated samples, the high-temperature phase of the compound was identified to be a separate compound with the chemical formula of $Mn_{1.08}Bi$. The ferro-to-paramagnetic transition upon heating to 628 K and para-to-ferromagnetic transition upon cooling to 613 K correspond respectively to the phase decomposition of MnBi $\rightarrow$ $Mn_{1.08}Bi$ + Bi and $Mn_{1.08}Bi$ $\rightarrow$ MnBi + Mn. Magnetic properties of the LTP, HTP, and QHTP obtained from the single crystals were compared to the previous data obtained from polycrystalline samples or thin films. For the QHTP single crystals, the saturation magnetization, M_s, at 4 K is 3.04 μ_B per Mn atom. This is 86% of the M_s of the LTP. A 300 K M_s appears to be 1.8 times larger than previously reported for polycrystalline samples or thin films. The anisotropy energy in the QHTP was found to be much larger than that of the LTP.

Brammeier *at al.* [124] were grown single crystals of MnBi by slowly cooling a melt of 10 at% Mn and 90 at% Bi from 410 °C to 272 °C, at which temperature the excess Bi was decanted by centrifuging. Each growth process produced dozens of crystals, often in the form of hexagonal platelets or prisms. The largest had hexagon “diameters” of 1–2 mm. Longer growth times yielded taller prisms, but not prisms with larger basal-plane areas. The magnetization was measured for fields applied parallel and perpendicular to the *c*-axis, both in a steady field as a function of temperature from 2 to 450 K, and as a function of field at constant temperature. Single crystals of MnBi were used for magneto-optic Kerr-angle spectroscopy and photoelectron spectroscopy.

c. Thin films. Thin films of MnBi mostly used for magneto-optical recording. The films can be prepared by vapor-deposition of a layer of Mn on a glass substrate followed by vapor-deposition of a layer of Bi. Subsequently, the composite system is annealed at temperatures ranging from 225 to 350 °C for several days [23]. Chen [22] proposed that more homogeneous films can be prepared by first depositing the Bi layer and subsequently the Mn layer. Favorable results were obtained with freshly cleaved mica substrates [23]. This material has the same basal plane symmetry as MnBi and makes it possible to have epitaxial growth. Thin MnBi films prepared on mica often were found to be essentially single crystals. Other types of substrate material can also be used (rock salt, quartz, teflon). It was found, in general, that the MnBi films have the *c*-axis oriented perpendicular to the substrate surface. The *a*-axis commonly adopts a random orientation, excepting films prepared on mica substrates. The MnBi film is usually overcoated with SiO. This overcoating protects the film against oxidation and contamination by moisture. Its presence is also of advantage with regard to the optimal properties of the thin-film system.

The first-ever reported preparation of MnBi thin film permanent magnets was in 1957 by Williams *et al.* [19], in which Mn and then a Bi layer were deposited on a glass substrate and then vacuum annealed for three days in the temperature range of 225–350 °C. Their large uniaxial anisotropy with easy *c* axis, large Faraday rotation and a large saturation magnetization at room temperature have made the α-MnBi thin films a rare-earth-free magnetic material for several applications, such as high-density recording, magneto-optic applications, magnetic storage and erasable magnetic holography applications.

Single-crystal MnBi films of thickness ranging from 2500 to 260 Å were grown epitaxially on mica substrates by vacuum deposition followed by a prolonged annealing procedure by Chen [125,126]. The *c* axis of these films was perpendicular to the plane of the film. Magnetic hysteresis in the direction along the *c* axis has been measured by both the magneto-optic method and the torque magnetometer technique. The hysteresis loop shows an abrupt decrease in magnetization as the field is reduced from positive saturation to a critical value. This critical field is positive in films thicker than 1200 Å. The coercive force of the films varies from 200 Oe to 2 kOe as film thickness decreases. The field required to saturate the films is 3.7 kOe and is approximately identical for all films. The dynamic flux reversal properties of these films were measured using a magneto-optical technique. The switching coefficient S_w was found to be 0.067 Oe·s. The experimental results suggest that the flux reversal in these films is not by domain rotation, but by the motion of the domain wall.

Usually, thin films for MO recording are prepared by evaporation or sputtering several thin alternating layers of Mn and of Bi followed by annealing to produce single-phase MnBi. The crystallite size of MnBi films, thus prepared, depends strongly on the annealing time and the temperature. Since the annealing time required for a complete reaction decreases with decreasing film thickness, the thinner MnBi film is expected to have smaller crystallites. The smaller crystallite size the higher density magneto-optical recording might be achieved. To obtain small crystallite MnBi films of a given thickness Masuda *et al.* [127] prepared multilayers of a thin MnBi double film by alternately evaporated Bi and Mn metals in a vacuum. These films were then annealed for as short time as possible but sufficient for a complete growth of MnBi. The MnBi com-

posite films, thus prepared, were found to possess a crystallite size of about 1000 Å which is too large for high-density recording.

The desire to enhance the magnetocrystalline anisotropy of MnBi thin films has been the driving force for researchers to try various techniques to grow high-quality films, such as magnetron sputtering, e-beam evaporation, and molecular beam epitaxy. One such technique, to prepare highly textured MnBi thin films, is via the pulsed laser deposition (PLD) method. The PLD allows the thin film preparation at temperatures as low as room temperature. Following this method, Zhou *et al.* reported the preparation of highly textured MnBi thin films [128]. Increasing the film thickness showed a better crystalline texture along the *c*-axis. The Bi layer was crucial for the growth of the textured MnBi and the column-like structures consist of many MnBi grains that are in the nanometer scale. On the other hand, depositing Mn as the first layer was met with several obstacles. It required more power from the source for the deposition of the Mn layer as the melting point of Mn is much higher than that of Bi. Besides, there were no observable phenomena of the preferential growth in the Mn thin film. Hence, the Bi layer turns out to be the better selection. Furthermore, annealing temperature played an important role in bringing out the texture and enhancing the magnetic properties of the MnBi. The films annealed between 340 and 350 °C showed the highest MnBi intensity under the XRD. The Rietveld refinement shows 85 wt% of the LTP-MnBi phase. This number is much lower than the values discussed in the bulk section because of the presence of the additional Bi in the first Bi layer. When examined for its magnetic anisotropy, the MnBi thin film showed large coercivity (15 kOe) at room temperature, which further increased up to 25.3 kOe at 100 °C. This positive temperature coefficient makes MnBi a unique magnetic system that can potentially replace NdFeB magnets at higher temperatures.

d. MnBi *nanoparticles*. MnBi has shown large coercivity at the bulk and thin film structures. Similar, or even better, results can be expected from the nanostructures of MnBi. Furthermore, a positive temperature coefficient for the coercivity makes MnBi a unique magnetic system and its energy density surpassed that of NdFeB magnets at higher temperatures. This makes MnBi a good candidate for the hard-magnetic part of the hard/soft composite for the exchange coupling [129]. Hence, material researchers have attempted several methods to synthesize MnBi nanoparticles with a facile and environmentally friendly method.

The attainment of nanostructured MnBi was reported by Kang *et al.* [130] at the nominal eutectic composition ($(MnBi)_5Bi_{95}$). Rapid solidification of the Mn–Bi binary composition, followed by annealing, was found to produce regular nanorods of LTP MnBi embedded in a Bi matrix. Transmission electron microscopy (TEM) studies revealed well-separated (7 vol.%) nanorods with dimensions 10 nm diameter ×30 nm length that were regularly self-assembled along the hexagonal basal plane axial directions of large Bi grains [130]. High-resolution TEM revealed atomically coherent contact between the basal planes of the MnBi and Bi phases but incoherent bonding along the *c* axes due to a very large lattice constant difference between the two phases. Elevated-temperature magnetic measurement confirmed a large Curie temperature T_C reduction to 520 K for these nanorods, relative to T_C = 633 K found for bulk MnBi. A large coercivity, over 16 kOe at 300 K, with a positive temperature coefficient was observed. In agreement with bulk results, ac susceptibility measurements show a spin reorientation around 90 K coincident with an abrupt decrease in the coercivity with decreasing temperature. The high coercivity at 300 K is attributed to a mixture of nucleation and pinning mechanisms for magnetic reversal. Later Kang *et al.* [131] investigated MnBi nanoparticles in a Bi matrix appeared in rapidly solidified Mn_xBi_{1-x} alloys for x = 0.05 and 0.10. They found that microstructural differences underlie diverse magnetic behavior: $Mn_{0.05}Bi_{0.95}$ alloys has well-separated nanorods along the basal plane axial directions of Bi, while $Mn_{0.10}Bi_{0.90}$ consists of MnBi nanorods and submicron-sized MnBi grains. The Curie transition of $Mn_{0.10}Bi_{0.90}$ is T_C = 630 K with a second-order thermodynamic character, while $Mn_{0.05}Bi_{0.95}$ nanorods exhibit a reduced and hysteretic T_C = 520 K. Magnetic field annealing fosters (00*n*) the alignment of the MnBi phase. $Mn_{0.10}Bi_{0.90}$ also shows alignment of the Bi matrix by a proposed templating mechanism.

Lam *et al.* fabricated MnBi nanoparticles using high energy ball-milling method [129]. First, a high-quality ingot was prepared by arc melting Mn and Bi with an atomic ratio of 55:45 ($Mn_{55}Bi_{45}$). The ingot was then crushed into smaller pieces, which were then ball-milled into nanoparticles. The size of the particles was largely dependent on the time of milling. Increasing the time of milling from 0.5 to 2 h reduced the particle size to about 25 nm. However, there was no noticeable reduction in the particle size for milling time > 4 h. The milling time also affected the magnetic properties of the sample because the magnetic properties of a material depend on its grain size. It was found that the coercivity of the specimen increased drastically from 7 to 16 kOe when the milling time was increased from 0.5 to 2 h. There was a smaller increment in the coercivity, from 16 to 17 kOe, when milled for 4 hours. After this, there was a noticeable decrease in the coercivity as the specimen was milled for 8 h. Though 4 h of milling gave larger grain and particle sizes, the largest coercivity at this milling time made it the optimal milling time for highly coercive $Mn_{55}Bi_{45}$. The M_s of the sample steadily increases with the increase in the milling time. This opposite behavior between the M_s and the coercivity is due to the presence of the larger volume fraction of the ferromagnetic MnBi when the specimen was milled for longer time, whereas the presence of more non-ferromagnetic compo-

nent, at shorter milling time, isolates the ferromagnetic components, thus increasing the coercivity of the specimen.

6.2. Constitution of MnBi

Up to now, no single-phase of MnBi with high H_c has been made by using convention methods such as arc-melting, mechanical milling and sintering, mainly due to the fact that Mn tends to segregate from the Mn–Bi liquid below the peritectic temperature. On the other hand, some authors argued that the effect of the substitution of manganese by some elements might be perspective way to improve the physical properties of MnBi as a permanent magnet. For example, the M–H data (at room temperature) on $Mn_{0.75}Ni_{0.25}Bi_{0.5}Sb_{0.5}$ sample indicates that the maximum magnetization (at 1.75 T) increases substantially to 38.8 emu/g compared to about 22 emu/g in MnBi prepared under similar conditions. The substitution possibly prevents segregation of Mn and thus results in the formation of a larger concentration of the magnetic phase.

e. Thin films. Kharel *et al.* investigated the structural, magnetic and magneto-transport properties of Mn substituted by Pt ($Mn_{55-x}Pt_xBi_{45}$) [132] and Fe ($Mn_{55-x}Fe_xBi_{45}$) [133] thin films. The coercivity of the Pt-alloyed thin films increases and the saturation magnetization decreases as the Pt concentration increases. The anisotropy field increases as a function of Pt concentration, too but the coercivity increases more rapidly than the anisotropy field [132]. This indicates an enhanced domain-wall pinning, caused by increased interstitial disorder due to the occupancy of regular Mn sites by Pt. The same mechanism explains the reduced magnetization. All samples exhibit a large extraordinary Hall effect with anomalous Hall coefficient about an order of magnitude larger than the ordinary Hall coefficient. Fe doping has produced a significant change in the magnetic properties of the samples including the decrease in saturation magnetization and magneto-crystalline anisotropy and increase in coercivity [133]. Although the magnetization shows a smooth decrease with increasing Fe concentration, the coercivity jumps abruptly from 8.5 to 22 kOe as Fe content changes from 4 to 5%, but the change in coercivity is small as the concentration goes beyond 5%. The temperature dependence of resistivity shows that the samples with low Fe concentration (≤ 4%) are metallic, but the resistivity increases unexpectedly as the concentration reaches 5%, where the resistance increases with decreasing temperature below 300 K. First-principle calculations [133] suggest that the observed magnetic properties can be understood as the consequences of competing ferromagnetic and antiferromagnetic exchange interactions between the interstitial atom and the rest of the MnBi lattice.

Kharel *et al.* [134] investigated the Kondo effect and electron-transport behavior of Pt-substituted MnBi thin films. They found that MnBi-Pt system exhibits a low-temperature Kondo resistance minimum in a strong ferromagnetic material with a Curie temperature well above room temperature. The system shows a positive magnetoresistance, which is unusual for Kondo systems. First-principles calculations show that Mn atoms displaced to the bipyramidal interstitial sites are antiferromagnetically coupled to the Mn atoms on their regular lattice sites. Both the Kondo effect and the positive magnetoresistance were explained as the consequences of local spin correlations involving Mn atoms displaced to interstitial sites by Pt doping.

The MnBi–MnSb system has been intensely investigated over the years using both polycrystalline bulk samples and thin film specimens. Ahlborn *et al.* [135] investigated the magnetic moment as a function of temperature for the full compositional range between pure MnSb and pure MnBi. The authors found the existence of a single ferromagnetic phase with a NiAs-type structure (LTP) only for Sb-rich compounds ($x > 0.7$). For all other compositions, the authors observed the coexistence of more than one crystallographic phase. The crystallographic phases for low concentration of Sb ($0.05 \le x \le 0.15$) in the MnBi–MnSb system were studied by Göbel *et al.* [136,137]. These authors found a stable orthorhombic (ORT) phase up to temperatures of 720 K. This phase is similar to the crystallographic structure first proposed by Andersen *et al.* [138] for their $MnBi_{0.9}Sb_{0.1}$ polycrystalline samples. Based on neutron scattering measurements [138] and the magnetic measurements [135] of $MnBi_{0.9}Sb_{0.1}$ the authors found that the magnetic moments form a spiral along the *c*-axis at room temperature. The growth, magnetic, and magneto-optical properties of MnBi–MnSb films for the Sb rich compositions were investigated by Takahashi *et al.* [139] and Wang *et al.* [140]. They found a significant excess of Mn, up to 60 at.%, was necessary to obtain positive uniaxial magnetic anisotropy in thin films [139].

Fang *et al.* [141,142] fabricated $MnBiRE_{0.1}$ (RE = Dy, Sm) alloy films, which exhibit perpendicular anisotropy, with thickness ranging from 60 to 1200 nm by the thermal evaporation method diffraction analysis has shown that the samples exhibit low-temperature phase (LTP) MnBi with a NiAs-type structure when the thicknesses of samples are less than 250 nm, however, the Bi_3Mn_2 phase, which is non-magnetic, also appears when the thicknesses are larger than 250 nm. The magnetic measurements have revealed that the saturation magnetization M_s = 46–78 emu/g, remanence ratio r = 0.67–0.99, coercive force H_c = 3.2–7.3 kOe, and magnetic energy product $(BH)_{max}$ = 3.3–14.3 MG·Oe, depend on the film thickness. The coercive force H_c reaches a maximum when d = 400 nm.

The effects of Ga-doping on the microstructure and magnetic properties of MnBi alloys were investigated recently by Yang *et al.* [143]. They show that the room temperature coercivities of $Mn_{55}Bi_{45-x}Ga_x$ after ball milling increased from 1.43 T for $x = 0$ to 1.66 T for $x = 5$, while the saturation magnetization decreased from 60.7 Am^2/kg ($x = 0$) to 45.1 Am^2/kg ($x = 5$). The maximum energy pro-

duct $(BH)_{max}$ of $Mn_{55}Bi_{44}Ga$ powders reached 7.87 MG·Oe. The Curie temperature of the $Mn_{55}Bi_{45-x}Ga_x$ alloys increased from 633 K to 658 K with increasing Ga concentration in the range of $0 \le x \le 5$.

f. Bulk MnBi. The most efforts in forming solid solutions of MnBi with other elements have been done for thin films of MnBi to improve magneto-optical recording properties. However, to create good permanent magnets we need to improve magnetic properties of MnBi in the bulk. In fact, the properties needed to improve in the films for magneto-optics and bulk for permanent magnets are different. The major problem in the former case is the preparation of a single-phase of MnBi. As we mentioned above, due to Mn segregating from the MnBi liquid at the peritectic temperature of 719 K and the slow diffusion of Mn through MnBi, it is difficult to obtain single-phase MnBi using conventional synthesis techniques [7,114,144]. Numerous attempts have been made for the purpose of obtaining single-phase MnBi, such as arc melting and rapid solidification methods [112,115], but formation of Mn precipitations and Bi matrix could not be avoided [145]. At present, no single-phase MnBi has been prepared. In order to oversee this impediment, many efforts have been made to stabilize MnBi by varying its stoichiometry or by alloying it with a third element like Cu, Al, Nb, Si, etc., without any success [29,51,146].

Rednic *et al.* [147] reported to obtain almost single-phase in Sb substituted MnBi. Four samples belonging to $MnSb_{1-x}Bi_x$ ($x = 0$, 0.2,0.5 and 0.95) system were prepared by argon arc melting method. The alloys obtained by the substitution of Sb with Bi in MnSb have the same hexagonal crystallographic NiAs structure type phase ($MnSb_{1-x}Bi_x$) corresponding to the parent compound MnSb and also observed for MnBi. They found the presence of some pure Bi atoms in the investigated samples due to the segregation of Bi during the preparation process. The pure Bi phase is quite small comparing to $MnSb_{1-x}Bi_x$ phase, except for $x = 0.95$ where it succeeds the nickel-arsenide structure type phase. Unfortunate, authors did not investigated the magnetic properties of the compounds and restricted themselves to the x-ray photoelectron spectra (XPS).

Saha *et al.* [145] examined the effect of partial substitution of Bi with rare earth elements on the magnetic properties of MnBi. $MnBi_{1-x}R_x$ (R = Nd, Dy) were prepared by mechanically alloying powders of the constituent elements at liquid nitrogen temperature followed by heat treatment. They found that in $MnBi_{1-x}Nd_x$, the coercivity (at room temperature) increases from 0.7 kOe to 6.6 kOe for $x = 0.0$ and 0.3, respectively. In $MnBi_{1-x}Dy_x$ the coercivity increases from 0.7 to 7.9 kOe for $x = 0.0$ and 0.3. The increase in coercivity may be in part due to the increase in the crystal field anisotropy as Nd or Dy is introduced and in part due to the finer particle size. A magnet made from MnBi shows coercivity of 17 kOe. The saturation induction is 1.55 kG. The significantly higher coercivity achieved in Ref. 145 is most likely due to the much finer particle size obtained by an extended period of ball milling. The obtained coercivity value is even higher than 16 kOe achieved by Kishimoto *et al.* [148] where an optimum grinding condition was established to achieve maximum coercivity.

6.3. Nanocomposite magnetic materials

Research has shown that the energy product of a magnetic material is dependent on its saturation magnetization (M_s) and coercivity (H_c). It is a challenge to synthesize a magnetic material that simultaneously exhibits large M_s and H_c, as the former is a property of a soft-magnet whereas the latter is a hard-magnetic property. A promising technique to promote both the above-mentioned properties in a magnetic material is via “exchange coupling”, where soft and hard-magnetic materials are fused together to give a good interface between them [46]. Research has shown that exchange coupling between magnetically soft and hard materials can give a large energy product, given that the parameters are maintained within a certain limit.

Nanocomposite magnetic materials are the mix of hard magnetic phase with high magnetocrystalline anisotropy and soft magnetic phase with high saturation magnetization in nanoscale. The optimal magnetic properties can be acquired via ferromagnetic coupling effect between the grains of the two phases. The micromagnetic simulations predicted $(BH)_{max}$ of 25 MG·Oe in MnBi/Co nanocomposite magnet [149] and of 25.13 MG·Oe in MnBi/α-Fe systems [150].

g. MnBi/(Fe,Co) *systems*. It is known that some Mn atoms in the MnBi lattice are antiferromagnetically aligned resulting in overall reduction of magnetization. To achieve strong ferromagnetic exchange coupling between MnBi and Fe domains, the effect of antiferromagnetically coupled Mn atoms must be quenched. Some authors try to develop a composite of MnBiX, where MnBi is the hard phase exchanged coupled with X = Fe or Co soft phases. The concept is to take advantage of MnBi’s exceptionally high coercivity at high temperatures and use soft phases such as Fe(Co) to amend its weak magnetization thus creating a magnet with high energy product at high temperatures. Here, element X is doped to the MnBi crystal lattice to prompt the ferromagnetic exchange coupling between Mn atoms of the MnBi lattice as well as across the MnBi and Fe or Co domains [151]. In an ideal situation, as simulated by Li’s group using micro-magnetic finite element method and assuming a perfect ferromagnetic exchange coupling, the α-MnBi-Fe(Co) composite can exhibit a $(BH)_{max}$ as high as 40 MG·Oe [150]. Such impressive potential inspired intensive theoretical and experimental investigations. Indirect evidence that this strategy can work was found in MnAl alloy, which is similar to MnBi: both have hexagonal structures, easy axis parallel to the *c*-axis, and large coercive fields up to 300 °C. Earlier, Matsumoto *et al.* [152] have reported that doping MnAl with a small amount of

transition metals can double the magnetization. Such a significant increase in magnetization lends direct support for substituting the Mn atoms responsible for the antiferromagnetism.

MnBi thin films grow with strong columnar texture leading to robust out-of-plane magnetic anisotropy. By comparison, most soft magnetic thin films possess in-plane anisotropy due to shape anisotropy. The perpendicularly exchange-coupled configuration of α-MnBi/Co_xFe_{1-x} bilayers with Co at the interface leads to a significant energy-product enhancement. The pure α-MnBi film shows strong perpendicular anisotropy with out-of-plane coercivity of 1.6 T and saturation magnetization of 0.8 T. By comparison, MnBi (20 nm)/Co (3 nm) and MnBi (20 nm)/Co (5 nm) bilayer films both exhibit reduced coercivity and enhanced remanence while maintaining a relatively square loop, indicating that an exchange coupling is established between the MnBi and Co films.

Gao *et al.* [151] explore the interfacial energy differences between AFM and FM magnetic-moment alignments across the interface for MnBi/Co_xFe_{1-x} exchange-coupled layers used density functional theory. They found that α-MnBi will ferromagnetically exchange couple with Co, but not with Fe. It is also possible for α-MnBi to ferromagnetically exchange couple with Fe–Co alloy, but the amount of Fe cannot be more than 50 at%. For the Co case, the maximum thickness of Co layer is only about 2 nm. The most striking feature of the present hard/soft exchange-coupled films is the significant enhancement of the nominal maximum energy product $(BH)_{max}$. Figure 24 shows the energy products for MnBi/Co, MnBi/$Co_{0.7}Fe_{0.3}$, MnBi/$Co_{0.3}Fe_{0.7}$, and MnBi/Fe bilayers with different soft-layer thicknesses according to Gao *et al.* [151]. For all soft-layer compositions Co_xFe_{1-x}, $(BH)_{max}$ initially increases sharply with the soft layer thickness, reaches a maximum, and eventually decreases. The $(BH)_{max}$ of

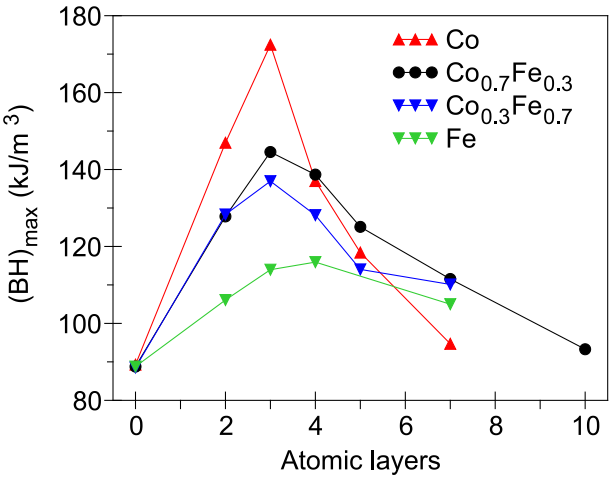

Fig. 24. $(BH)_{max}$ of MnBi/CoxFe$_{1-x}$ bilayers for different soft-layer compositions and thicknesses [151].

pure MnBi films are 89(±6.2) kJ/m^3, and it increases to 172(±8.6) kJ/m^3 for 3 nm Co and then gets reduced to 95(±5.7) kJ/m^3 for 7 nm Co.

In parallel to the thin film approach, researchers have been working on nano-synthesis of MnBi–FeCo core-shell. Xu and Hong [153] used a magnetic self-assembly process to obtain exchange-coupled hard/soft α-MnBi/Fe-Co core/shell structured composites. Their MnBi particles were obtained through milling of coarse powder, and the FeCo shell was coated later through chemical synthesis. Henkel plots of the obtained α-MnBi/FeCo core-shell particles indicated exchange coupling dominates in α-MnBi/FeCo (95/5 wt%) composites, and magnetostatic interaction dominates in α-MnBi/FeCo (90/10 wt%) composites, indicating the limitation in the amount of the soft phase can that can be coupled. Dai and Ren [154] also demonstrated the exchange coupling between α-MnBi and FeCo using nano-synthesis method. The difference is that the α-MnBi nanoparticle was obtained using metal-redox method and FeCo nanowires were electrospun. In both cases, the overall energy product of the composite was less than 6 MG·Oe, mainly due to the large amount of impurities that are difficult to remove after the solutionbased chemical synthesis.

h. MnBi/NdFeB *systems*. Today, bonded NdFeB-based permanent magnets have been widely used due to their good magnetic properties. However, their undesirable thermal stability is still a major concern (see Fig. 23) in some practical application such high-temperature motors. As a result, a kind of magnet, named bonded hybrid magnets, in which two or more different magnetic powders were mixed together, had been developed [155–158]. In the common hybrid magnets, ferrite with positive coercivity temperature coefficient was used to compensate the NdFeB, leading to an improved thermal stability. Unfortunately, the poor coercivity of the ferrite undermines the application of such hybrid magnets. The α-MnBi compounds possess a high coercivity and pronounced positive temperature coefficient below 300 °C, therefore, the bonded hybrid MnBi/NdFeB magnets are expected to bear good magnetic properties and thermal stability.

Cao *et al.* [155] investigated magnetic properties and thermal stability of the MnBi/NdFeB (MnBi = 0, 20, 40, 60, 80, and 100 wt%) bonded hybrid magnets prepared by spark plasma sintering (SPS) technique. Effect of MnBi content on the magnetic properties of the hybrid magnets was studied. With increasing MnBi content, the coercivity of the MnBi/NdFeB hybrid magnets increases rapidly, while the remanence and maximum energy product drops simultaneously. Thermal stability measurement on MnBi magnet, NdFeB magnet, and the hybrid magnet with 20 wt% MnBi indicates that both the NdFeB magnet and the MnBi/NdFeB hybrid magnet have a negative temperature coefficient of coercivity, while the MnBi magnet has a positive one. The $(BH)_{max}$ of the MnBi/NdFeB magnet (MnBi = 20 wt%) is 5.71 MG·Oe at 423 K, which is much higher than

3.67 MG·Oe of the NdFeB magnet, indicating a remarkable improvement of thermal stability.

Zhang *et al.* [157] fabricated and investigated anisotropic hybrid bonded magnets MnBi/NdFeB (MnBi = 0, 20, 40, 60, 80, and 100 wt%). Figure 25(a), (b) shows the room temperature magnetic properties and density of the anisotropic MnBi/NdFeB hybrid bonded magnets as a function of MnBi content [157]. The pure anisotropic NdFeB bonded magnet possesses the best coercivity (H_c), and maximum energy product $(BH)_{max}$ of 1122.36 kA·m^{-1}, and 92.34 kJ·m^{-3}, respectively, while the pure MnBi bonded magnet has the lowest values of the magnetic properties. As MnBi content increases, the coercivity and maximum energy product of the hybrid magnets all drop simultaneously. The coercivity temperature coefficients of the MnBi/NdFeB bonded magnets (in the temperature range of 293–398 K) are shown in Fig. 25(c). Throughout this temperature range, the pure MnBi bonded magnet exhibits a positive coercivity temperature coefficient of 0.61% K^{-1}, while pure NdFeB bonded magnet possesses a negative one of –0.59% K^{-1}. As for the hybrid bonded magnets, the coercivity temperature coefficient remains negative but slightly improves compared with pure NdFeB bonded magnet. For the hybrid bonded magnet with 80 wt% MnBi, the coercivity temperature coefficient is about –0.32% K^{-1}, indicating that the MnBi/NdFeB bonded magnets exhibit better thermal stability in the temperature range of 293–398 K. So the MnBi/NdFeB bonded magnets could be a good candidate for high-temperature applications.

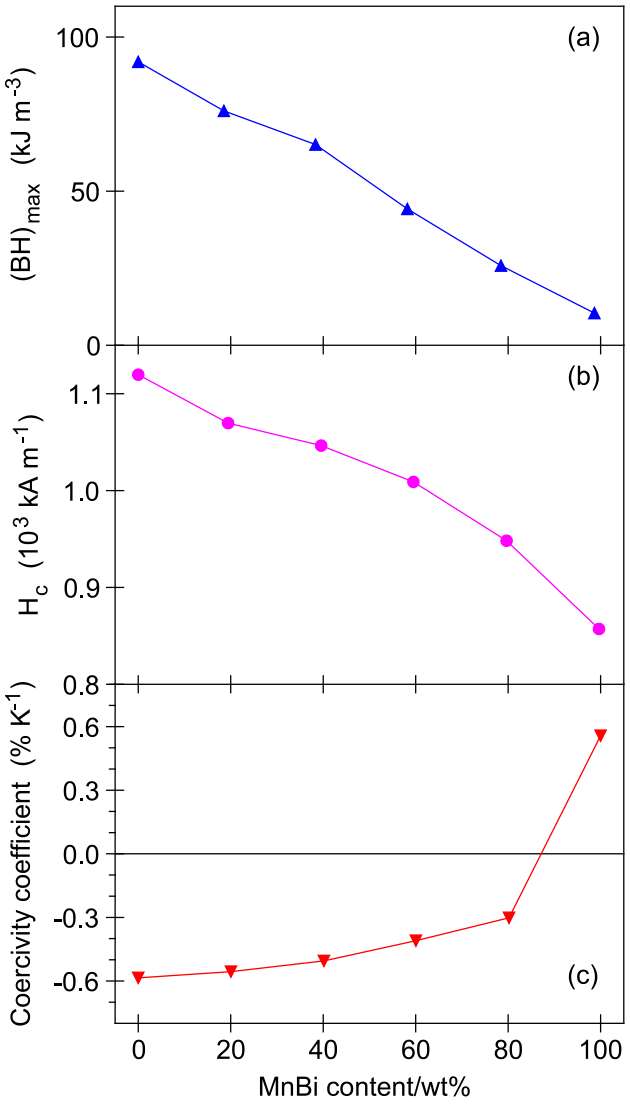

Fig. 25. Dependence of maximum energy product $(BH)_{max}$ (a), coercivity H_c (b), and coercivity temperature coefficient (in the temperature range 293–398 K) (c) on MnBi content in MnBi/NdFeB bonded magnets. (Data extracted from Ref. 157).

Similar results were obtained also in the case of anisotropic MnBi/SmFeN hybrid bonded magnets by Zhang *et al.* [156]. For the pure MnBi magnet, the coercivity is increased from 10.76 kOe at 293 K to 16.5 kOe at 373 K. For the hybrid magnet with 40 wt% MnBi, the coercivity is increased by 19% compared to pure SmFeN magnet at 373 K. In the temperature range of 293–373 K, the coercivity temperature coefficient of the hybrid magnets changes gradually from –0.42%/K for the pure SmFeN magnet to –0.11 %/K for the magnet with 80 wt% MnBi, and becomes 0.67 %/K for the pure MnBi magnet.

Anisotropic bulk hybrid MnBi/NdFeB magnets have been prepared also by Ma *et al.* [158] via improved warm compaction and sintering techniques. It was found that a proper processing and suitable composition lead to high - density bulk magnets that possess advantages of both the MnBi and NdFeB phases. An energy product $(BH)_{max}$ of 10 MG·Oe has been obtained at NdFeB content of 50 wt%, which is substantially higher than any reported values of the energy density-bulk MnBi-based magnets. Meanwhile, the hybrid magnets also have a better thermal stability at elevated temperatures compared to the NdFeB magnets due to the positive temperature coefficient of coercivity of the MnBi phase.

7. Conclusions

It is apparent that ultrastrong magnets with superior thermal and chemical stability are essential to address ongoing and future technological needs in society. In particular, escalating demand for cheaper, smaller, and more powerful motors and generators for consumer, military, and energy applications such as wind turbines and hybrid or electric vehicles will require a steady and secure supply of high-energy product permanent magnets. In this context, the rare earth elements, in their role as enabling chemical components of high-energy product magnets, will remain extremely important. On the other hand, it is anticipated that the so-called “rare-earth crisis” will subside-somewhat-over the next decade as new rare-earth element supplies are secured, new permanent magnetic materials are developed, and new device and motor designs that utilize lower amounts of rare-earth permanent magnets are implemented. While there currently exists a shortage of rare

earth production capacity, it is important that create new concepts for the creation of low- or rare-earth-free permanent magnet materials will remain an important pursuit in magnetic materials science.

Although MnBi is a good candidate for the rare-earth-free permanent magnet, it is very difficult to prepare the single-phase compound using conventional methods such as arc-melting, mechanical milling and sintering, which is mainly due to that Mn tends to segregate from the Mn–Bi liquid below the peritectic temperature 719 K. So far, many methods have been tried to avoid the segregation. For example, MnBi has been grown under microgravity condition by greatly reducing the separation of Mn and Bi. Another way to prepare homogeneous MnBi alloys is by using melt-spinning, and LTP MnBi can be obtained with subsequent annealing. A high purity LTP MnBi prepared using this method [115], but with relatively small H_c (only 0.2 T at room temperature). The grinding method can increase the H_c [119], but the saturation magnetization decreased severely after grind due to the impurity phase. Up to now, no single-phase MnBi with high H_c has been made by melt-spinning. On the other hand, the effect of the substitution of manganese by some elements might be the perspective way to improve the physical properties of MnBi as a permanent magnet. For example, the M–H data (at room temperature) on $Mn_{0.75}Ni_{0.25}Bi_{0.5}Sb_{0.5}$ sample indicates that the maximum magnetization (at 1.75 T) increases substantially to 38.8 emu/g compared to about 22 emu/g in MnBi prepared under similar conditions. The substitution possibly prevents segregation of Mn and thus results in the formation of a larger concentration of the magnetic phase.

Another approach to improve the energy product of α-MnBi is to take advantage of its large magnetocrystalline anisotropy and exchange couple the α-MnBi with a soft phase such as Fe, Co or FeCo. In an ideal situation, with assuming a perfect the ferromagnetic exchange coupling, the α-MnBi–Fe(Co) composite can exhibit a $(BH)_{max}$ as high as 40 MG·Oe [159]. Such impressive potential inspired intensive theoretical and experimental investigations. Indirect evidence that this strategy can work was found in MnAl alloy. Matsumoto *et al.* have reported that doping MnAl with a small amount of transition metals can double the magnetization.

Today, bonded NdFeB-based permanent magnets have been widely used due to their good magnetic properties. However, their undesirable thermal stability is still a major concern in some practical application such high-temperature motors. As a result, a kind of magnet, named bonded hybrid magnets, in which two or more different magnetic powders were mixed together, had been developed [155–158]. In the common hybrid magnets, ferrite with a positive coercivity temperature coefficient was used to compensate the NdFeB, leading to improved thermal stability. Unfortunately, the poor coercivity of the ferrite undermines the application of such hybrid magnets. α-MnBi compound possesses a high coercivity and pronounced positive temperature coefficient below 300 °C, therefore, the bonded hybrid MnBi/NdFeB magnets are expected to bear good magnetic properties and thermal stability.

Modern first-principles band-structure methods are able to calculate the electronic structure, Fermi surface, orbital dependence of the cyclotron masses, and extremal cross-sections of the Fermi surface, magneto-optical Kerr spectra, x-ray magnetic circular dichroism, temperature dependence of the magneto-crystalline anisotropy of MnBi with good accuracy. It was found the SO interaction strongly affects the shape of the Fermi surface changing the size and even the topology of some sheets of the FS in MnBi. The inclusion of the Coulomb repulsion in a frame of the LSDA+SO+U method also changes of the theoretically calculated FS in MnBi. The effect of the Coulomb correlations change the energy band structure of MnBi in two ways. First, it leads to a shift of the Mn d occupied states downward by U_{eff} / 2 and empty Mn 3d states to a shift upwards by this amount ($U_{\text{eff}} = U - J$) relative to the Fermi energy. Second, the Coulomb correlations enhance an effective spin-orbit coupling constant. The splitting of the energy bands is enhanced more than two times after the inclusion of the Coulomb repulsion for some states near Fermi energy. The inclusion of the Coulomb repulsion U also changes the orbital character of the electronic states at the Fermi surface.

The band-structure theory, based on density-functional theory in the local spin-density approximation with spin-orbit and Coulomb repulsion taken into account, explains the measured Kerr effect of MnBi very well. The experimentally observed record Kerr rotation of –1.6° is directly given by band-structure theory. First-principles calculations even predict a larger Kerr angle for pure MnBi than was measured. However, the experimental peak at 3.4 eV in the Kerr angle comes out smaller in our *ab initio* LSDA+SO calculations. A tentative explanation of this feature can be sought in the influence of the Coulomb electron-electron correlations. The LSDA+SO+U calculations produce the second high-energy negative peak at 3.4 eV in good agreement with the experimental measurements. Although the Kerr effect is a rather complicated function of the diagonal and off-diagonal optical conductivities, band-structure theory nevertheless provides very practical insight into the origin of the Kerr effect in MnBi. The huge Kerr effect in MnBi can be understood within a simplified model, based on the maximal 3d magnetic moment on Mn, the nearly maximal SO coupling of Bi, as well as the strong hybridization between the manganese d bands and the bismuth p states. The magneto-optically active states are mainly the p states of Bi.

Both magneto-optical effects and MAE have a common origin in the spin-orbit coupling and exchange splitting. Thus, a close connection between the two phenomena seems plausible. At room temperature, MnBi is known to have an extremely high magneto-crystalline energy. This de-

creases, however, rapidly with decreasing temperature and posses zero at a spin-reorientation transition temperature $T_{SR} \sim 90$ K. The magnetic moment turns from the along the hexagonal axis at room temperature to a direction in the basal plane below T_{SR}. With increasing temperature above room temperature, the anisotropy energy increases rapidly and reaches its maximum at about 500 K and then rapidly decreases above this temperature.

The LSDA+SO approximation gives the value of MAE equal to –2.2 meV/unit cell at zero temperate. This value is an order of magnitude larger than experimentally estimated one 0.13 meV/unit cell [18,87]. Besides, the LSDA+SO approximation shows that the easy direction of the magnetization is in the basal plane for all temperature range and, therefore, provides no explanation of the spin-reorientation observed experimentally at the $T_{SR} \sim 90$ K. On the other hand, the LSDA+SO+U approach provides the value of the MAE at 0 K of 0.39 meV which is in better agreement with the experiment in comparison with the LSDA+SO approach. The inclusion of the Coulomb correlations in a frame of the LSDA+SO+U approach provides correct easy magnetization direction for the whole temperature interval. The LSDA+SO+U theory produces the MAE in a very good agreement with the experiment in the 150 to 450 K temperature range.

The SO coupling of Bi is equally responsible for the large MAE as is the exchange splitting of Mn. When the exchange splitting on Bi is set to zero, the MAE remains almost as it is. But when we do the same for the exchange splitting on Mn, the MAE totally vanishes. If we set the SO coupling on Mn to zero, the MAE does not change very much. On the other hand, when the SO coupling on Bi is zero, the MAE almost disappears. The scaling of the SO coupling of Bi by a factor of 2.0 leads to a tremendous increase of the MAE by factor of 5, thereby illustrating the leading role of the SO interaction at the Bi site for the MAE in this compound as it was observed in the case of the MO spectra. The SO interaction and Coulomb correlations also strongly affects the shape of the FS by changing the size and even the topology of some sheets of the FS in MnBi.

For a large amount of properties that have been discussed in this paper, no prior theoretical or experimental studies have been performed. With high-quality single crystal samples already available, the opportunity to perform the initial experimental study of many properties discussed above becomes feasible and therefore our theoretical predictions can be tested.

Acknowledgments

This research is supported by an Energy Innovation Hub funded by the U.S. DOE and by the Office of Basic Energy Science, Division of Materials Science and Engineering. Ames Laboratory is operated for the U.S. DOE by Iowa State University under contract DE-AC02–07CH11358.

1. J. Yang, K. Kamaraju, W. Yelon, and W. James, *Appl. Phys. Lett.* **79**, 1846 (2001).
2. G.Q. Di, S. Iwata, S. Tsunashima, and S. Uchiyama, *J. Meteorol. Soc. Jpn.* **16**, 113 (1992).
3. R.R. Heikes, *Phys. Rev.* **99**, 446 (1955).
4. U. Rüdiger and G. Güntherodt, *J. Appl. Phys.* **88**, 4221 (2000).
5. J.B. Yang, W.B. Yelon, W.J. James, Q. Cai, M. Kornecki, S. Roy, N. Ali, and P. I'Heritier, *J. Phys.: Condens. Matter* **14**, 6509 (2002).
6. T. Chen and W.E. Stutius, *IEEE Transact. Magnet.* **10**, 581 (1974).
7. A.F. Andersen, W. Hälg, P. Fischer, and E. Stoll, *Acta Chem. Scand.* **21**, 1543 (1967).
8. F. Heusler, *Z. Angew. Chern.* **17**, 260 (1904).
9. E. Bekier, *Int. Z. Metallogr.* **7**, 83 (1914).
10. N. Parravano and U. Perret, *Gazz. Chern. Ital.* **451**, 390 (1915).
11. S. Hilpert and T. Dieckmann, *Ber. Deut. Chern. Ges.* **44**, 2831 (1911).
12. U. Furst and F. Halla, *Z. Phys. Chern. B* **40**, 285 (1938).
13. E. Montignie, Bull. Soc. Chim. **5**, 343 (1938).
14. F. Halla and E. Montignie, *Z. Phys. Chern. B* **42**, 153 (1939).
15. C. Guillaud, *PhD Thesis*, University of Strasbourg, Strasbourg, France (1943).
16. E. Adams, *Rev. Mod. Phys.* **25**, 306 (1953).
17. T. Hihara and Y. Köi, *J. Phys. Soc. Jpn.* **29**, 343 (1970).
18. W.E. Stutius, T. Chen, and T.R. Sandin, *AIP Conf. Proc.* **18**, 1222 (1974).
19. H.J. Williams, R.C. Sherwood, F.G. Foster, and E.M. Keller, *J. Appl. Phys.* **28**, 1181 (1957).
20. L. Mayer, *J. Appl. Phys.* **29**, 1003 (1958).
21. L. Mayer, *J. Appl. Phys.* **31**, 3845 (1960).
22. D. Chen, *J. Appl. Phys.* **42**, 3625 (1971).
23. K.H.J. Buschow, in: *Ferromagnetic Materials*, E.P. Wohlfarth and K.H.J. Buschow (eds.), Amsterdam, North-Holland (1988), vol. 4, p. 588.
24. D. Huang, X.W. Zheng, C.P. Luo, H.S. Yang, and Y.J. Wang, *J. Appl. Phys.* **75**, 6351 (1993).
25. G.Q. Di and S. Uchiyama, *Phys. Rev. B* **53**, 3327 (1996).
26. K. Harder, D. Menzel, T. Widmer, and J. Schoenes, *J. Appl. Phys.* **84**, 3625 (1998).
27. R. Coehoorn and R. de Groot, *J. Phys. F* **15**, 2135 (1985).
28. Z.W. Wang and M.C. Huang, *Chinese Phys. Lett.* **10**, 612 (1993).
29. R.F. Sabiryanov and S.S. Jaswal, *Phys. Rev. B* **53**, 313 (1996).
30. P.M. Oppeneer, V.N. Antonov, T. Kraft, H. Eschrig, A.N. Yaresko, and A.Y. Perlov, *J. Appl. Phys.* **80**, 1099 (1996).
31. Y.A. Uspenskii, E.T. Kulatov, and S.V. Halilov, *Phys. Rev. B* **54**, 474 (1996).
32. J. Köhler and J. Kübler, *J. Phys.: Condens. Matter* **8**, 8681 (1996).
33. J. Köhler and J. Kübler, *Physica B* **402**, 237 (1997).
34. L.V. Burkova, S.G. Ovchinnikov, V.A. Seredkin, and V.Y. Yakovchuk, *J. Magn. Magn. Mater.* **195**, 531 (1999).

35. P. Ravindran, A. Delin, P. James, B. Johansson, J.M. Wills, R. Ahuja, and O. Eriksson, *Phys. Rev. B* **59**, 15680 (1999).
36. M.Q. Tan, X.M. Tao, and S.N. Bao, *Chinese Phys.* **9**, 55 (2000).
37. P. Mavropoulos, K. Sato, R. Zeller, P.H. Dederichs, V. Popescu, and H. Ebert, *Phys. Rev. B* **69**, 054424 (2004).
38. J.C. Zheng and J.W. Davenport, *Phys. Rev. B* **69**, 145415 (2004).
39. H. Weng, Y. Kawazoe, and J. Dong, *Phys. Rev. B* **74**, 085205 (2006).
40. M. Li, T. Ariizumi, K. Koyanagi, and S. Suzuki, *Jpn. J. Appl. Phys.* **46**, 3455 (2007).
41. B. Sanyal and O. Eriksson, *J. Appl. Phys.* **103**, 07D704 (2008).
42. L. Kahal and M. Ferhat, *J. Appl. Phys.* **107**, 043910 (2010).
43. J.N. Goncalves, V.S. Amaral, J.G. Correia, and A.M.L. Lopes, *Phys. Rev. B* **83**, 104421 (2011).
44. P. Kharel, P. Thapa, P. Lukashev, R.F. Sabirianov, E.Y. Tsymbal, D.J. Sellmyer, and B. Nadgorny, *Phys. Rev. B* **83**, 024415 (2011).
45. V.P. Antropov, V.N. Antonov, L.V. Bekenov, A. Kutepov, and G. Kotliar, *Phys. Rev. B* **90**, 054404 (2014).
46. K. Patel, J. Zhanga, and S. Ren, *Nanoscale* **10**, 11701 (2018).
47. K. Cenzual, L. Gelato, M. Penzo, and E. Parthe, *Acta Crystallogr.* **47**, 433 (1991).
48. Y.B. Yang, X.G. Chen, S. Guo, A.R. Yan, Q.Z. Huang, M.M. Wu, D.F. Chen, Y.C. Yang, and J.B. Yang, *J. Magn. Magn. Mater.* **330**, 106 (2013).
49. M.A. McGuire, H. Cao, B.C. Chakoumakos, and B.C. Sales, *Phys. Rev. B* **90**, 174425 (2014).
50. N.A. Zarkevich, L.-L. Wang, and D.D. Johnson, *Apl. Mater.* **2**, 032103 (2014).
51. P.R. Bandaru, T.D. Sands, Y. Kubota, and E.E. Marinero, *Appl. Phys. Lett.* **72**, 2337 (1998).
52. J. Smit and H.P.J. Wijn, *Ferrites*, Philips Technical Library, Eindhoven (1959).
53. J. Schoenes, in: *Electronic and Magnetic Properties of Metals and Ceramics*, R.W. Cahn, P. Haasen, and E.J. Kramer (eds.) Verlag Chemie, Weinheim (1992), vol. 3A, p. 147, K.H.J. Buschow (vol. editor).
54. R. Kubo, *J. Phys. Soc. Jpn.* **12**, 570 (1957).
55. C.S. Wang and J. Callaway, *Phys. Rev. B* **9**, 4897 (1974).
56. V.N. Antonov, A.I. Bagljuk, A.Y. Perlov, V.V. Nemoshkalenko, Vl.N. Antonov, O.K. Andersen, and O. Jepsen, *Fiz. Nizk. Temp.* **19**, 689 (1993) [*Low Temp. Phys.* **19**, 494 (1993)].
57. V. Antonov, B. Harmon, and A. Yaresko, *Electronic Structure and Magneto-Optical Properties of Solids*, Kluwer, Dordrecht (2004).
58. J. Kunes and P.M. Oppeneer, *Phys. Rev. B* **67**, 024431 (2003).
59. J.P. Perdew and A. Zunger, *Phys. Rev. B* **23**, 5048 (1981).
60. V.I. Anisimov, J. Zaanen, and O.K. Andersen, *Phys. Rev. B* **44**, 943 (1991).
61. L. Hedin, *Phys. Rev. A* **140**, A796 (1965).
62. W. Metzner and D. Vollhardt, *Phys. Rev. Lett.* **62**, 324 (1989).
63. T. Pruschke, M. Jarell, and J.K. Freericks, *Adv. Phys.* **44**, 187 (1995).
64. A. Georges, G. Kotliar, W. Krauth, and M.J. Rozenberg, *Rev. Mod. Phys.* **68**, 13 (1996).
65. A.N. Yaresko, V.N. Antonov, and P. Fulde, *Phys. Rev. B* **67**, 155103 (2003).
66. O. Bengone, M. Alouani, P. Blöchl, and J. Hugel, *Phys. Rev. B* **62**, 16392 (2000).
67. V.I. Anisimov and O. Gunnarsson, *Phys. Rev. B* **43**, 7570 (1991).
68. I.V. Solovyev, P.H. Dederichs, and V.I. Anisimov, *Phys. Rev. B* **50**, 16861 (1994).
69. P.H. Dederichs, S. Blügel, R. Zeller, and H. Akai, *Phys. Rev. Lett.* **53**, 2512 (1984).
70. W.E. Pickett, S.C. Erwin, and E.C. Ethridge, *Phys. Rev. B* **58**, 1201 (1998).
71. M. Cococcioni and S. de Gironcoli, *Phys. Rev. B* **71**, 035105 (2005).
72. K. Nakamura, R. Arita, Y. Yoshimoto, and S. Tsuneyuki, *Phys. Rev. B* **74**, 235113 (2006).
73. F. Aryasetiawan, K. Karlsson, O. Jepsen, and U. Schonberger, *Phys. Rev. B* **74**, 125106 (2006).
74. E. Antonides, E.C. Janse, and G.A. Sawatzky, *Phys. Rev. B* **15**, 1669 (1997).
75. D. van der Marel, G.A. Sawatzky, and F.U. Hillebrecht, *Phys. Rev. B* **53**, 206 (1984).
76. M. Springer and F. Aryasetiawan, *Phys. Rev. B* **57**, 4364 (1998).
77. T. Kotani, *J. Phys.: Condens. Matter* **12**, 2413 (2000).
78. F. Aryasetiawan, M. Imada, A. Georges, G. Kotliar, S. Biermann, and A.I. Lichtenstein, *Phys. Rev. B* **70**, 195104 (2004).
79. I.V. Solovyev and M. Imada, *Phys. Rev. B* **71**, 045103 (2005).
80. T. Miyake, F. Aryasetiawan, and M. Imada, *Phys. Rev. B* **80**, 155134 (2009).
81. T. Miyake and F. Aryasetiawan, *Phys. Rev. B* **77**, 085122 (2008).
82. K. Nakamura, R. Arita, and M. Imada, *J. Phys. Soc. Jpn.* **77**, 093711 (2008).
83. T. Miyake, L. Pourovskii, V. Vildosola, S. Biermann, and A. Georges, *J. Phys. Soc. Jpn.* **77**, Suppl. C, 99 (2008).
84. L. Zhiqiang, L. Helie, L. Wuyan, Z. Zhi, and Z. Qingqi, *Solid State Commun.* **79**, 791 (1991).
85. J.B. Yang, Y.B. Yang, X.G. Chen, X.B. Ma, J.Z. Han, Y.C. Yang, S. Guo, A.R. Yan, Q.Z. Huang, M.M. Wu, and D.F. Chen, *Appl. Phys. Lett.* **99**, 082505 (2011).
86. K. Koyama, Y. Mitsui, and K. Watanabe, *Sci. Technol. Adv. Mater.* **9**, 024204 (2008).
87. N. Vast, B. Siberchicot, and P.G. Zerah, *J. Phys.: Condens. Matter* **4**, 10469 (1992).
88. K. Yosida, A. Okiji, and S. Chikazumi, *Prog. Theor. Phys.* **33**, 559 (1965).
89. M. Cinal, D.M. Edwards, and J. Mathon, *Phys. Rev. B* **50**, 3754 (1994).
90. V.P. Antropov, L. Ke, and D. Aberg, *Solid State Commun.* **194**, 35 (2014).
91. M. Montalti, A. Credi, L. Prodi, and M.T. Gandolfi, in: *Handbook of Photochemistry*, N.J. Turro (ed.), Taylor and Francis Group, Boca Raton, FL (2006), p. 629.
92. W. Reim and J. Schoenes, in: *Ferromagnetic Materials*, E.P. Wohlfarth and K.H.J. Buschow (eds.), North-Holland, Amsterdam (1990), vol. 5, p. 133.

93. L. Uba, S. Uba, V.N. Antonov, A.N. Yaresko, T. Slezak, and J. Korecki, *Phys. Rev. B* **62**, 13831 (2000).
94. J. Cui, M. Kramer, L. Zhou, F. Liu, A. Gabay, G. Hadjipanayis, B. Balasubramanian, and D. Sellmyer, *Acta Mater.* **158**, 118 (2018).
95. Z.W. Liu, R.V. Ramanujan, and H.A. Davies, *J. Mater. Res.* **23**, 2733 (2008).
96. E.F. Kneller and R. Hawig, *IEEE Trans. Magn.* **27**, 3588 (1991).
97. R. Skomski and J.M.D. Coey, *Phys. Rev. B* **48**, 15812 (1993).
98. R. Coehoorn, D.B. Mooji, and C. DeWaard, *J. Magn. Magn. Mater.* **80**, 101 (1989).
99. G.C. Hadjipanayis, *J. Magn. Magn. Mater.* **200**, 373 (1999).
100. H. Zeng, J. Li, J.P. Liu, Z.L. Wang, and S. Sun, *Nature* **420**, 395 (2002).
101. X. Rui, Z. Sun, L. Yue, Y. Xu, D.J. Sellmyer, Z. Liu, D. Miller, and J. Shield, *J. Magn. Magn. Mater.* **305**, 76 (2006).
102. E. Adams, W.M. Hubbard, and A.M. Syeles, *J. Appl. Phys.* **23**, 1207 (1952).
103. J.B. Yang, W.B. Yelon, W.J. James, Q. Cai, S. Roy, and N. Ali, *J. Appl. Phys.* **91**, 7866 (2002).
104. X. Li, C.-H. Wu, Y.-J. Lee, Y.-L. Huang, C.-L. Huang, J.-L. Tsai, T.-H. Wu, T. Chen, J.V. Lierop, and K.-W. Lin, *Minerals, Metals Mater. Soc.* **48**, 1426 (2019).
105. J. Frenkel and J. Dorfman, *Nature* **126**, 274 (1930).
106. V.H. Gottschalk, *Bureau of Mines R.I.* **83**, 3268 (1935).
107. R. Dean and F. Davis, *U.S. Patent 2.239* (1941), p. 145.
108. L. Néel, *Compt. Rend.* **24**, 1550 (1947).
109. E.C. Stoner and E.P. Wohlfarth, *Trans. Roy. Soc. (London)* **240**, 599 (1948).
110. C. Kittel, *Phys. Rev.* **73**, 810 (1948).
111. C. Kittel, *Rev. Modern Phys.* **21**, 541 (1949).
112. H. Yoshida, T. Shima, T. Takahashi, and H. Fujimori, *Mater. Transact. Jpn. Institute Metals* **40**, 455 (1999).
113. X. Guo, A. Zaluska, Z. Altounian, and J.O. Stromolsen, *J. Mater. Res.* **5**, 2646 (1990).
114. B.W. Roberts, *Phys. Rev.* **104**, 607 (1956).
115. X. Guo, Z. Altounian, and J.O. Stromolsen, *J. Appl. Phys.* **69**, 6067 (1991).
116. N.V.R. Rao, A.M. Gabay, and G.C. Hadjipanayis, *J. Phys. D* **46**, 062001 (2013).
117. N.V.R. Rao, A.M. Gabay, W. Li, and G.C. Hadjipanayis, *J. Phys. D* **46**, 265001 (2013).
118. J. Cui, J.P. Choi, G. Li, E. Polikarpov, J. Darsell, N. Overman, M. Olszta, D. Schreiber, M. Bowden, T. Droubay, M.J. Kramer, N.A. Zarkevich, L.L. Wang, D.D. Johnson, M. Marinescu, I. Takeuchi, Q.Z. Huang, H. Wu, H. Reeve, N.V. Vuong, and J.P. Liu, *J. Phys.: Condens. Matter* **26**, 064212 (2014).
119. S. Saha, R.T. Obermyer, B.J. Zande, V.K. Chandhok, S. Simizu, S.G. Sankar, and J.A. Horton, *J. Appl. Phys.* **91**, 8525 (2002).
120. Y.B. Yang, X.G. Chen, R. Wu, J.Z. Wei, X.B. Ma, J.Z. Han, H.L. Du, S.Q. Liu, C.S. Wang, Y.C. Yang, Y. Zhang, and J.B. Yang, *J. Appl. Phys.* **111**, 07E312 (2012).
121. D.T. Zhang, W.T. Geng, M. Yue, W.Q. Liu, J.X. Zhang, J.A. Sundararajan, and Y. Qiang, *J. Magn. Magn. Mater.* **324**, 1887 (2012).
122. W.M. Yim and E.J. Stofko, *J. Appl. Phys.* **38**, 5211 (1967).
123. T. Chen, *J. Crystal Growth* **24/25**, 454 (1974).
124. D.P. Brammeier, J.-M. Park, C.G. Olson, I.R. Fisher, and D.W. Lynch, *J. Magn. Magn. Mater.* **283**, 95 (2004).
125. D. Chen, *J. Appl. Phys.* **37**, 1486 (1966).
126. D. Chen, *J. Appl. Phys.* **38**, 1309 (1967).
127. M. Masuda, I. Izawa, S. Yoshino, S. Shiomi, and S. Uchiyama, *Jpn. J. Appl. Phys.* **26**, 707 (1987).
128. D. Zhou, Y.-F. Zhang, X.-B. Ma, J.-Z. Han, M.-G. Zhu, C.-S. Wang, and J.-B. Yang, *Chin. Phys. Lett.* **32**, 127502 (2015).
129. N.M. Lam, T.M. Thi, P.T. Thanh, N.H. Yen, and N.H. Dan, *Mater. Transact.* **9**, 1404 (2015).
130. K. Kang, L.H. Lewis, and A.R. Moodenbaugh, *J. Appl. Phys.* **97**, 10K302 (2005).
131. K. Kang, A.R. Moodenbaugh, and L.H. Lewis, *Appl. Phys. Lett.* **90**, 153112 (2007).
132. P. Kharel, R. Skomski, R.D. Kirby, and D.J. Sellmyer, *J. Appl. Phys.* **107**, 09E303 (2010).
133. P. Kharel, X.Z. Li, V.R. Shah, N. Al-Aqtash, K. Tarawneh, R.F. Sabirianov, R. Skomski, and D.J. Sellmyer, *J. Appl. Phys.* **111**, 07E326 (2012).
134. P. Kharel, R. Skomski, P. Lukashev, R. Sabirianov, and D.J. Sellmyer, *Phys. Rev. B* **84**, 014531 (2011).
135. K. Ahlbom, K. Bärner, and W. Schröter, *Phys. Status Solidi A* **30**, 251 (1975).
136. H. Göbel, E. Wolfgang, and R. Harmas, *Phys. Status Solidi A* **34**, 553 (1976).
137. H. Göbel, E. Wolfgang, and R. Harmas, *Phys. Status Solidi A* **35**, 89 (1976).
138. A.F. Andersen, J.E. Engebretsen, and J. Refesnes, *Acta. Chem. Scand.* **26**, 175 (1972).
139. M. Takahashi, Y. Kikuchi, T. Tanaka, and T. Wakiyama, *IEEE Transact. Magn. Jpn.* **5**, 998 (1990).
140. Y.J. Wang, J.X. Shen, and Q. Tang, *J. Magn. Magn. Mater.* **74**, 365 (1988).
141. R. Fang, Q. Fang, S. Zhang, C. Peng, and D. Dai, *J. Appl. Phys.* **77**, 1178 (1995).
142. Q. Fang, R. Fang, S. Zhang, and D. Dai, *J. Magn. Magn. Mater.* **188**, 241 (1998).
143. Y. Yang, J.-W. Kim, P.-Z. Si, H.-D. Qian, Y. Shin, X. Wang, J. Park, O.L. Li, Q. Wu, H. Ge, C.J. Choi, *J. Allloys Compd.* **769**, 813 (2018).
144. J.M.N. van Goor and H. Zijlstra, *J. Appl. Phys.* **39**, 5471 (1968).
145. S. Saha, M.Q. Huang, C.J. Thong, B.J. Zande, V.K. Chandhok, S. Simizu, R.T. Obermyer, and S.G. Sankar, *J. Appl. Phys.* **87**, 6040 (2000).
146. J. Wang, *J. Magn. Magn. Mater.* **84**, 39 (1990).
147. L. Rednic, M. Coldea, V. Rednic, M. Neumann, and D. Benea, *Studia Universitatis Babes-Bolyal, Physica* **LIII**, 65 (2008).
148. M. Kishimoto and K. Wakai, *J. Appl. Phys.* **48**, 4640 (1977).
149. Y.Q. Li, M. Yue, T. Wang, Q. Wu, D.T. Zhang, and Y. Gao, *J. Magn. Magn. Mater.* **393**, 484 (2015).

150. Y.Q. Li, M. Yue, J.H. Zuo, D.T. Zhang, W.Q. Liu, J.X. Zhang, Z.H. Guo, and W. Li, *IEEE Trans. Magn.* **49**, 3391 (2013).
151. T.R. Gao, L. Fang, S. Fackler, S. Maruyama, X.H. Zhang, L.L. Wang, T. Rana, P. Manchanda, A. Kashyap, K. Janicka, A.L. Wysocki, A.T. N'Diaye, E. Arenholz, J.A. Borchers, B.J. Kirby, B.B. Maranville, K.W. Sun, M.J. Kramer, V.P. Antropov, D.D. Johnson, R. Skomski, J. Cui, and I. Takeuchi, *Phys. Rev. B* **94**, 060411 (2016).
152. M. Matsumoto, A. Morisako, and J. Ohshima, *J. Appl. Phys.* **69**, 5172 (1991).
153. X. Xu, Y.-K. Hong, J. Park, W. Lee, A.M. Lane, and J. Cui, *J. Solid State Chem.* **231**, 108 (2015).
154. Q. Dai, J.Q. Xiao, and S. Ren, *Nano Res.* **9**, 3222 (2016).
155. S. Cao, M. Yue, Y.X. Yang, D.T. Zhang, W.Q. Liu, J.X. Zhang, Z.H. Guo, and W. Li, *J. Appl. Phys.* **109**, 07A740 (2011).
156. D.T. Zhang, W.T. Geng, M. Yue, W.Q. Liu, Q.M. Lu, J.X. Zhang, Z.H. Guo, W. Li, J.A. Sundararajan, and Y. Qiang, *J. Appl. Phys.* **115**, 17A746 (2014).
157. D.-T. Zhang, P.-F. Wang, M. Yue, W.-Q. Liu, J.-X. Zhang, J.A. Sundararajan, and Y. Qiang, *Rare Met.* **35**, 471 (2016).
158. Y.L. Ma, X. Liu, V.V. Nguyen, N. Poudyal, M. Yue, and J.P. Liu, *J. Magn. Magn. Mater.* **411**, 116 (2016).
159. Y.Q. Li, M. Yue, J.H. Zuo, D.T. Zhang, W.Q. Liu, J.X. Zhang, Z.H. Guo, and W. Li, *J. Magn.* **18**, 245 (2013).

Низькотемпературні сплави MnBi: електронні та магнітні властивості, склад, морфологія і виготовлення
(Огляд)

В.М. Антонов, В.П. Антропов

Розглянуто велику різноманітність фізичних властивостей MnBi, які включають сильну спін-орбітальну взаємодію, аномальну температурну залежність коерцитивної сили та анізотропію магнітокристалічного поля, унікальні магнітооптичні властивості. Розглядаються питання природи електронних властивостей основного стану MnBi, електронна та магнітна структури, поверхня Фермі, магнітокристалічна анізотропія, рентгенівський магнітний дихроїзм. Обговорюються ключові експерименти такі, як оптичні та магнітооптичні вимірювання, вимірювання ефекту де Гааза–ван Альфена (dHvA), фотоемісія рентгенівського випромінювання та спектроскопія рентгенівського поглинання, а також рентгенівський магнітний циркулярний дихроїзм. Встановлено, що спін-орбітальна взаємодія та сильне кулонівське міжелектронне відштовхування мають вирішальне значення для поверхні Фермі, циклотронних мас, магнітооптичних властивостей та рентгенівського магнітного циркулярного дихроїзму. Детально проаналізовано мікроскопічне походження унікальної магнітокристалічної анізотропії та ефекту Керра у MnBi. Гігантський ефект Керра у MnBi викликано комбінацією великого магнітного моменту у марганці, великою спін-орбітальною взаємодією у вісмуті та сильною гібридизацією між марганцевими 3*d*- та вісмутовими 6*p*-станами. Магнітооптичними активними станами є в основному 6*p*-стани Bi. Показано, що залежність магнітокристалічної анізотропії від температури, яка спостерігається, може бути пояснена з урахуванням спін-орбітальної взаємодії разом з сильною кулонівською електрон-електронною взаємодією. Спін-орбітальна взаємодія у Bi та обмінне розщеплення у Mn однаково відповідальні за велику магнітокристалічну анізотропію у MnBi. Обговорено виготовлення, морфологія та склад низькотемпературних сплавів MnBi в об'ємі, тонких плівках та наночастинках. Розглянуто також нанокомпозитні матеріали MnBi з постійними магнітами на основі Co, Fe та $Nd_2Fe_{14}B$.

Ключові слова: кристалічна структура, магнітокристалічна анізотропія, магнітооптичні властивості, рентгенівський магнітний циркулярний дихроїзм.

Низкотемпературные сплавы MnBi: электронные и магнитные свойства, состав, морфология и изготовление
(Обзор)

В.Н. Антонов, В.П. Антропов

Рассмотрено огромное разнообразие физических свойств MnBi, которые включают сильное спин-орбитальное взаимодействие, аномальную температурную зависимость коэрцитивной силы и анизотропию магнитокристаллического поля, уникальные магнитооптические свойства. Рассматриваются вопросы природы электронных свойств основного состояния MnBi, электронная и магнитная структуры, поверхность Ферми, магнитокристаллическая анизотропия, рентгеновский магнитный дихроизм. Обсуждаются ключевые эксперименты такие, как оптические и магнитооптические измерения, измерения эффекта де Гааза–ван Альфена (dHvA), фотоэмиссия рентгеновского излучения и спектроскопия рентгеновского поглощения, а также рентгеновский магнитный циркулярный дихроизм. Установлено, что спин-орбитальное взаимодействие и сильное кулоновское межэлектронное отталкивание имеют решающее значение для поверхности Ферми, циклотронных масс, магнитооптических свойств и рентгеновского магнитного циркулярного дихроизма. Детально проанализированы микроскопическое происхождение уникальной магнитокристаллической анизотропии и эффекта Керра в MnBi. Гигантский эффект Керра в MnBi вызван комбинацией большого магнитного момента в марганце, большого спин-орбитального взаимодействия в висмуте и сильной гибридизацией между марганцевыми 3*d*- и висмутовыми 6*p*-состояниями. Магнитооптически активными состояниями являются в основном 6*p*-состояния Bi. Показано, что наблюдаемая зависимость магнитокристаллической анизотропии от температуры может быть объяснена с учетом спин-орбитального взаимодействия вместе с сильным кулоновским электрон-

электронным взаимодействием. Спин-орбитальное взаимодействие в Bi и обменное расщепление в Mn одинаково ответственны за большую магнитокристаллическую анизотропию в MnBi. Обсуждены изготовление, морфология и состав низкотемпературных сплавов MnBi в объеме, тонких пленках и наночастицах. Рассмотрены также нанокомпозитные материалы MnBi с постоянными магнитами на основе Co, Fe и $Nd_2Fe_{14}B$.

Ключевые слова: кристаллическая структура, магнитокристаллическая анизотропия, магнитооптические свойства, рентгеновский магнитный циркулярный дихроизм.